

STELLAR KINEMATICS IN THE COMPLICATED INNER SPHEROID OF M31: DISCOVERY OF SUBSTRUCTURE ALONG THE SOUTHEASTERN MINOR AXIS AND ITS RELATIONSHIP TO THE GIANT SOUTHERN STREAM

KAROLINE M. GILBERT¹, MARK FARDAL², JASONJOT S. KALIRAI^{1,3}, PURAGRA GUHATHAKURTA¹, MARLA C. GEHA^{4,5}, JEDIDAH ISLER^{6,7}, STEVEN R. MAJEWSKI⁸, JAMES C. OSTHEIMER⁸, RICHARD J. PATTERSON⁸, DAVID B. REITZEL⁹, EVAN KIRBY¹, AND MICHAEL C. COOPER¹⁰

Submitted to ApJ, Feb. 28 2007

ABSTRACT

We present the discovery of a kinematically-cold stellar population along the southeastern minor axis of the Andromeda galaxy (M31) that is likely the forward continuation of M31's giant southern stream. This discovery was made in the course of an on-going spectroscopic survey of red giant branch (RGB) stars in M31 using the DEIMOS instrument on the Keck II 10-m telescope¹¹. Stellar kinematics are investigated in eight fields located 9–30 kpc from M31's center (in projection). A likelihood method based on photometric and spectroscopic diagnostics is used to isolate confirmed M31 RGB stars from foreground Milky Way dwarf stars: for the first time, this is done *without* using radial velocity as a selection criterion, allowing an unbiased study of M31's stellar kinematics. The radial velocity distribution of the 1013 M31 RGB stars shows evidence for the presence of two components. The broad (hot) component has a velocity dispersion of $\sigma_v^{\text{sph}} = 129 \text{ km s}^{-1}$ and presumably represents M31's virialized spheroid. A significant fraction (19%) of the population is in a narrow (cold) component centered near M31's systemic velocity with a velocity dispersion that decreases with increasing radial distance, from $\sigma_v^{\text{sub}} = 55.5 \text{ km s}^{-1}$ at $R_{\text{proj}} = 12 \text{ kpc}$ to $\sigma_v^{\text{sub}} = 10.6 \text{ km s}^{-1}$ at $R_{\text{proj}} = 18 \text{ kpc}$. The spatial and velocity distribution of the cold component matches that of the “southeast shelf” predicted by the Fardal et al. (2007) orbital model of the progenitor of the giant southern stream. The metallicity distribution of the cold component matches that of the giant southern stream, but is about 0.2 dex more metal rich on average than that of the hot spheroidal component. We discuss the implications of our discovery on the interpretation of the intermediate-age spheroid population found in this region in recent ultra-deep *HST* imaging studies.

Subject headings: galaxies: substructure — galaxies: halo — galaxies: individual (M31) — stars: kinematics — techniques: spectroscopic

1. INTRODUCTION

In the current paradigm of hierarchical galaxy formation, massive galaxies are built up through a se-

¹ UCO/Lick Observatory, Department of Astronomy & Astrophysics, University of California Santa Cruz, 1156 High Street, Santa Cruz, California 95064; [kgilbert, jkalirai, raja, ekirby]@ucolick.org.

² Department of Astronomy, University of Massachusetts, Amherst, Massachusetts 01003; fardal@fcrao1.astro.umass.edu.

³ Hubble Fellow.

⁴ NRC Herzberg Institute of Astrophysics, 5701 West Saanich Road, Victoria, British Columbia, Canada V9E 2E7; marla.geha@nrc-cnrc.gc.ca.

⁵ Plaskett Fellow.

⁶ Fisk University/Vanderbilt University, Nashville, Tennessee 37325.

⁷ Visiting Student, University of California Santa Cruz; jcisler@ucolick.org.

⁸ Department of Astronomy, University of Virginia, PO Box 400325, Charlottesville, VA 22904-4325; srm4n@virginia.edu, jostheim@alumni.virginia.edu, rjp0i@virginia.edu.

⁹ Department of Physics & Astronomy, Knudsen Hall, University of California, Los Angeles, California 90095; reitzel@astro.ucla.edu.

¹⁰ Department of Astronomy, Campbell Hall, University of California, Berkeley, California 94720; cooper@astron.berkeley.edu.

¹¹Data presented herein were obtained at the W. M. Keck Observatory, which is operated as a scientific partnership among the California Institute of Technology, the University of California and the National Aeronautics and Space Administration. The Observatory was made possible by the generous financial support of the W. M. Keck Foundation.

ries of major and minor merger events (Searle & Zinn 1978; White & Rees 1978). Observations of galaxies at high redshift show that merging systems are common (e.g., Abraham et al. 1996; LeFevre et al. 2000; Conselice et al. 2003; Lotz et al. 2007), and large-scale simulations of galaxy formation in a cosmological context have successfully reproduced many of the observed properties of galaxies and galaxy clusters (e.g., Springel et al. 2005; Croton et al. 2006).

A consequence of hierarchical galaxy formation is that galactic stellar halos should be at least partially composed of tidal debris of past accretion events. Numerical simulations and semi-analytic models of stellar halo formation have made great strides toward understanding the properties of halos that are built up through tidal stripping of merging systems (e.g., Johnston et al. 1996; Johnston 1998; Helmi & White 1999; Helmi & de Zeeuw 2000; Bullock et al. 2001; Bullock & Johnston 2005). Detailed comparisons between observations and simulations are needed to determine the fraction of stellar halos that are made up of tidal debris and to better understand the formation of galaxies in general.

Recent discoveries of tidal streams in the stellar halos of the Milky Way (MW) and Andromeda (M31) galaxies are providing the most direct and detailed observational constraints on theories of stellar halo formation. Among the most prominent of these substructures are

the Sagittarius stream (Ibata et al. 1994; Majewski et al. 2003; Newberg et al. 2003), the Monoceros stream (Yanny et al. 2003; Rocha-Pinto et al. 2003), and the Magellanic stream (Mathewson et al. 1974) in the MW, and the giant southern stream (GSS; Ibata et al. 2001b) in M31. Additional substructures have been identified in M31 that are also likely remnants of past mergers, such as the northeast shelf (Ferguson et al. 2002; Ibata et al. 2004; Fardal et al. 2006), a secondary cold component in the same physical location as the giant southern stream (Kalirai et al. 2006a), and the various substructures identified with the disk of M31 (Ibata et al. 2005). Tidal disruption has also been observed in M31's satellite galaxies M32 and NGC 205 (Choi et al. 2002).

In addition to providing insight into theoretical models of stellar halo formation, the observed properties of tidal streams can be used to constrain the the galactic potential in which they are found if sufficient phase-space information is available (e.g., Johnston et al. 1999, 2002; Peñarrubia et al. 2006). Several attempts have been made to model the mass distribution of the MW using observed substructure, most of which have focused on the orbital properties of the Sagittarius stream (e.g., Ibata et al. 2001a; Helmi 2004; Martínez-Delgado et al. 2004; Johnston et al. 2005; Law et al. 2005; Fellhauer et al. 2006).

The GSS has been the focus of detailed modeling in M31. Imaging and photometry have revealed the physical extent of the GSS (Ferguson et al. 2002; McConnachie et al. 2003; Ferguson et al. 2006) and provided line-of-sight distances at various points along it (McConnachie et al. 2003), while spectroscopy has yielded the mean line-of-sight velocity and velocity dispersion of stream stars as a function of position (Ibata et al. 2004; Guhathakurta et al. 2006; Kalirai et al. 2006a). This phase-space information has motivated several groups to model the orbit of the progenitor of the GSS (Ibata et al. 2004; Font et al. 2006; Fardal et al. 2006, 2007). However, Fardal et al. (2006) concluded that the degree to which the GSS can be used to constrain M31's mass distribution is limited by the current measurement uncertainties in the distance to the stream and the lack of a clearly identified compact stellar concentration that might correspond to the dense remnant core of the stream's progenitor galaxy. Further observational constraints on the orbit of the progenitor of the GSS, such as tidal debris from other pericentric passages, are needed to make progress.

Towards this end, Fardal et al. (2007, hereafter F07) show that several of the observed features in M31 can be explained as the forward continuation of the GSS. Their model makes a few predictions that can be tested by observations, including the stellar velocity distributions in the northeast and western shelves, and also predicts that there may be a weaker shelf on the eastern side of the galaxy. This last shelf is expected to be most easily visible near the southeast minor axis of M31¹².

This paper presents new substructure in M31's southeast minor-axis region at the expected location of the F07

¹² Although this shell feature is expected to span a $\sim 180^\circ$ range in position angle, covering the eastern half of the galaxy, it will likely only be observable in the southeast due to its overlap with the much denser northeast shelf and M31's disk (see Fig. 12).

southeast shelf and displaying the distinct kinematic profile predicted by their orbital model. The substructure was discovered as part of an on-going Keck/DEIMOS spectroscopic study of the dynamics and metallicity of RGB stars in the inner spheroid and outer halo of M31 (see Gilbert et al. 2006, and references therein). The photometric and spectroscopic data used in this analysis are described in § 2. The criteria for selection of M31 RGB stars are discussed in § 3. The kinematics of the RGB population (first the combined data set and then the individual fields) are characterized in § 4. The spatial trends and general properties of the dynamically hot spheroid and cold substructure populations are discussed in § 5 and § 6, respectively. The possible physical origins of the substructure are explored in § 7, including its likely relation to M31's GSS. The relevance of the newly discovered substructure to the Brown et al. (2003) intermediate-age population in the spheroid of M31 is discussed § 8. The main conclusions of the paper are summarized in § 9.

2. DATA

The data set discussed in this paper is drawn from photometry and spectroscopy of several fields on/near the southeastern minor axis of M31. The locations of the fields are shown in Figures 1 and 2. They span a projected radial distance from M31's center of $R_{\text{proj}} \sim 9$ kpc to $R_{\text{proj}} \sim 30$ kpc (Table 1). A brief explanation of the data sets and reduction is included below. A more detailed discussion of the observational and data reduction methods employed in our M31 survey can be found in Guhathakurta et al. (2005, 2006), Kalirai et al. (2006a,b), and Gilbert et al. (2006).

2.1. Photometry

Photometry for the majority of the fields comes from MegaCam images in the g' and i' bands obtained with the 3.6-m Canada-France-Hawaii Telescope (CFHT)¹³. The program SExtractor (Bertin & Arnouts 1996) was used for object detection, photometry, and morphological classification (via the `stellarity` parameter). The instrumental g' and i' magnitudes were transformed to Johnson-Cousins V and I magnitudes based on observations of Landolt photometric standard stars (Kalirai et al. 2006a).

Photometry for a0, the outermost field discussed in this paper, comes from the photometry/astrometry catalogs of Ostheimer (2002), which are derived from images obtained with the Mosaic camera on the Kitt Peak National Observatory (KPNO)¹⁴ 4-m telescope in the Washington System M and T_2 bands and the intermediate-width DDO51 band. This combination of filters allows photometric selection of stars that are likely to be M31 red giant branch (RGB) stars rather than MW dwarf stars (e.g., Palma et al. 2003). The DDO51 filter is centered

¹³ MegaPrime/MegaCam is a joint project of CFHT and CEA/DAPNIA, at the Canada-France-Hawaii Telescope which is operated by the National Research Council of Canada, the Institut National des Sciences de l'Univers of the Centre National de la Recherche Scientifique of France, and the University of Hawaii.

¹⁴ Kitt Peak National Observatory of the National Optical Astronomy Observatory is operated by the Association of Universities for Research in Astronomy, Inc., under cooperative agreement with the National Science Foundation

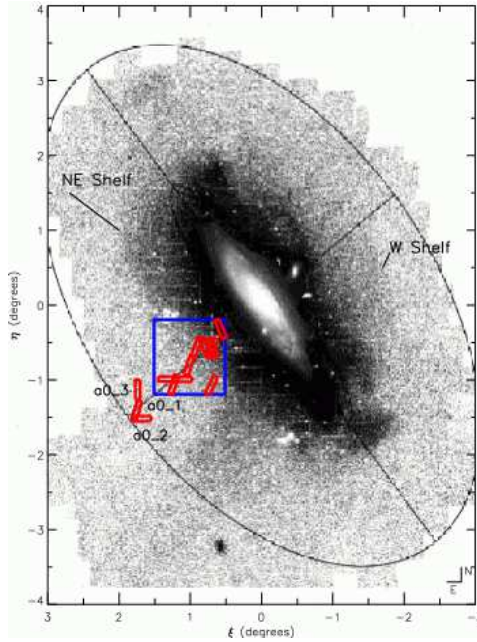


FIG. 1.— Sky positions of the fields discussed in this paper. The blue square represents the position and area of the CFHT/MegaCam image (Fig. 2). The red rectangles approximate the size and position angle of the DEIMOS spectroscopic slitmasks. The three masks nearest the outer ellipse are in field a0. The remaining masks are identified in Figure 2. The star count map comes from Ibata et al. (2005), and is in the standard M31-centric coordinates (ξ, η). The outer ellipse represents a 55 kpc radius along the major axis, with a flattening of 3.5. The major and minor axes of M31 are indicated by straight lines. The giant southern stream is the obvious overdensity of stars south of M31's center.

at a wavelength of 5150 Å with a width of ~ 100 Å, and includes the surface-gravity sensitive Mg *b* and MgH stellar absorption features, which are strong in dwarf stars but weak in RGB stars. Based on a star's position in the ($M - DDO51$) versus ($M - T_2$) color-color diagram, it is assigned a probability of being an M31 RGB star. Johnson-Cousins *V* and *I* magnitudes were derived from the *M* and *T₂* magnitudes using the photometric transformation relations in Majewski et al. (2000). Use of the DDO51 photometry to screen for likely M31 RGB stars greatly increases the efficiency of the spectroscopic observations, suppressing the number of selected MW dwarf stars by a factor of 5 (Guhathakurta et al. 2005).

2.2. Spectroscopy

2.2.1. Slitmasks Design and Observations

Objects in fields drawn from the CFHT/MegaCam images were selected for Keck/DEIMOS spectroscopy based on *I* magnitude and the SExtractor morphological criterion **stellarity** (Kalirai et al. 2006b). Objects in field a0 were selected on the basis of *I* magnitude, morphological criteria (DAOPHOT parameters **chi** and **sharp**), and probability of being an M31 RGB star (based on *M*, *T₂*, and DDO51 photometry, § 2.1). Pre-selection of likely M31 RGB stars is vital for efficient study of the sparse outer parts of the M31 halo. The inner fields (such as the fields drawn from the CFHT/MegaCam images) contain a relatively high surface density of M31 RGB stars, so the RGB to MW dwarf star ratio is high even without pre-selection of RGB candidates.

For the purposes of the analysis in this paper, data are

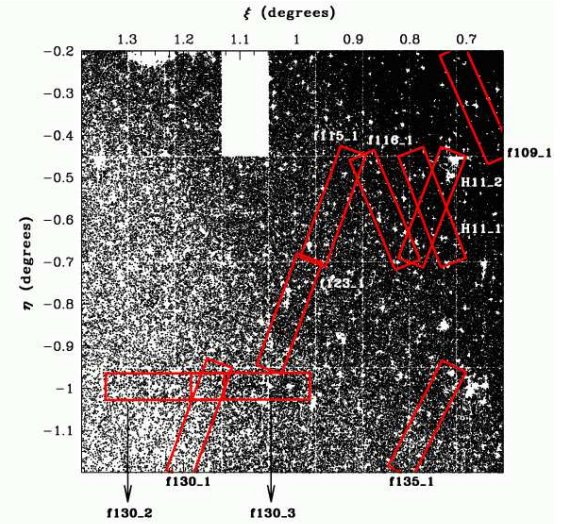


FIG. 2.— Starcount map derived from CFHT/MegaCam photometry in a single pointing with the 36-CCD mosaic (§ 2.1). The orientation of this map is the same as Figure 1. The size and positions of the masks designed from the CFHT/MegaCam photometry are shown as red rectangles. The three a0 masks were based on photometry from the KPNO 4-m telescope and are to the southeast (bottom left), beyond the limit of this image. There is an apparent edge in the density of star counts in the image, running from the upper left to the lower right and passing through field f123; this feature will be discussed in § 7.1.

classified according to fields, rather than spectroscopic masks. In general, a “field” refers to the area covered by a single MegaCam CCD ($\sim 15' \times 6.5'$, Fig. 2); there can be one or more overlapping DEIMOS masks ($16' \times 4'$) in a single field. For example, masks H11_1 and H11_2 are both part of field H11. There are two exceptions: (1) the a0 field refers to a single Mosaic pointing, which covers a $35' \times 35'$ area, and (2) two of the f130 masks each span a couple of MegaCam CCDs, but since they were chosen to overlap with the f130_1 mask, they have been labelled f130_2 and f130_3.

Most of the fields were observed in Fall 2005 [f109, f115, f116, f123, f130 (1 mask), and f135] using the Keck II telescope and the DEIMOS instrument with the $1200 \text{ line mm}^{-1}$ grating. Masks in fields a0 and H11 were observed in Fall 2002 and 2004, and 2 of the 3 masks in field f130 were observed in Fall 2006 (Table 1). The central wavelength for most masks was $\lambda 7800$ Å, yielding the spectral coverage $\lambda\lambda 6450 - 9150$ Å. The only exceptions were the a0_1 and a0_2 masks observed in 2002, which had a central wavelength of $\lambda 8550$ Å and a spectral coverage of $\lambda\lambda 7200 - 9900$ Å. The $1200 \text{ line mm}^{-1}$ grating has a dispersion of 0.33 Å pix^{-1} , the scale in the spatial direction is $0''.12 \text{ pix}^{-1}$, and the scale in the dispersion direction is $0''.21 \text{ pix}^{-1}$. Slits had a width of $1''$. Each mask was observed for a total of 1 hour, with the exception of field f109 which was observed for 3 hours.

2.2.2. Spectroscopic Data Reduction

The spectra were reduced and analyzed using a modified version of the **spec2d** and **spec1d** software developed by the DEEP2 team at the University of Califor-

TABLE 1
DETAILS OF SPECTROSCOPIC OBSERVATIONS AND BASIC RESULTS.

Mask	Projected Radius (kpc)	Pointing center: α_{J2000} (h,m,s)	δ_{J2000} (°:':")	PA (°E of N)	Date of Obs. (UT)	# Sci. targets ^a	# of M31 Stars ^{a,b}
f109_1	9	00:45:46.75	+40:56:53.8	23.90	2005 Aug 29	208	169
H11_1	12	00:46:21.02	+40:41:31.3	21.0	2004 Sep 20	139	89
H11_2	12	00:46:21.02	+40:41:31.3	-21.0	2004 Sep 20	138	88
f116_1	13	00:46:54.53	+40:41:29.5	22.60	2005 Aug 28	199	149
f115_1	15	00:47:32.71	+40:42:00.9	-20.0	2005 Aug 28	191	114
f123_1	18	00:48:05.57	+40:27:16.3	-20.0	2005 Aug 28	171	104
f135_1	18	00:46:24.88	+40:11:35.5	-27.0	2005 Aug 29	146	99
f130_1	22	00:49:11.97	+40:11:45.3	-20.0	2005 Aug 28	108	52
f130_2	23	00:49:37.49	+40:16:07.0	90.0	2006 Nov 21	115	43
f130_3	20	00:48:34.59	+40:16:07.0	90.0	2006 Nov 22	124	41
a0_1	31	00:51:51.32	+39:50:21.4	-17.9	2002 Aug 16	89	25
a0_2	31	00:51:29.59	+39:44:00.8	90.0	2002 Oct 12	89	32
a0_3	29	00:51:50.46	+40:07:00.9	0.0	2004 Jun 17	90	26

^a A number of targets were observed on two different masks: the total number of unique science targets/M31 RGB stars in fields H11, f130 and a0 is therefore less than the reported number. There were 2 M31 RGB stars with duplicate observations in H11, 8 in f130, and 8 in a0.

^b The number of M31 RGB stars is defined as the number of stars that are identified as secure and marginal M31 RGB stars by the Gilbert et al. (2006) diagnostic method, without the use of the radial velocity diagnostic ($\langle L_i \rangle_\phi > 0$, § 3).

nia, Berkeley¹⁵; these routines perform standard spectral reduction steps, including flat-fielding, night-sky emission line removal, and extraction of the two-dimensional spectra. Reduced one-dimensional spectra are cross-correlated with a library of template stellar spectra to determine the redshift of the object. Each spectrum was visually inspected and assigned a quality code based on the number and quality of absorption lines. Only spectra with at least two spectral features (even if one of them is marginal) are considered to have secure redshift measurements. A heliocentric correction is applied to the measured radial velocities based on the sky position of the mask and the date and time of the observation. The heliocentric velocities are not corrected for the changing component of solar motion across our fields; our innermost and outermost fields are separated by 1.5° along the southeast minor axis, which corresponds to only a 1.6 km s⁻¹ velocity change.

Spectra in field a0 were reduced using the original reduction techniques briefly outlined above. Detailed discussions of the spectral reduction techniques, quality determination, and S/N measurements used in our survey can be found in Guhathakurta et al. (2006) and Gilbert et al. (2006). Spectra in the remainder of the fields were reduced using several improvements to the reduction pipeline. A greater number of stellar templates are used for the spectral cross-correlation, and the template library has been modified to include spectral templates from the Keck II telescope's Echellete Spectrograph and Imager (ESI) instead of Sloan Digital Sky Survey (SDSS) spectral templates. The ESI templates were chosen because they more closely match the resolution of the observed spectra. The position of the atmospheric A-band in the observed spectrum is used to correct the observed radial velocity for imperfect centering of the star in the slit (Kalirai et al. 2007, in prep; Sohn et al. 2007).

Field H11 has been presented by previous papers (Kalirai et al. 2006a; Brown et al. 2003, 2006a). The radial velocity histogram of H11 presented in this paper has $\approx 50\%$ more M31 RGB stars than the previously published sample, due to the recent recovery of spectra from two CCDs that were not included in these papers and the improvements in the data reduction process described above.

3. SELECTING A SAMPLE OF M31 RED GIANTS

The largest source of contaminants in our spectroscopic survey are foreground MW dwarf stars. Background galaxies are easy to identify and remove from the sample on the basis of their spectra and redshifts. However, the radial velocity distribution of MW dwarf stars overlaps that of M31 RGB stars, making identifying individual stars as M31 red giants or MW dwarfs problematical. We use the diagnostic method detailed in Gilbert et al. (2006) to separate M31 RGB stars from MW dwarf star contaminants. The method uses empirical probability distribution functions to estimate the likelihood a given star is an M31 red giant based on five photometric and spectroscopic diagnostics:

- The radial velocity of the star.
- Photometry in the M , T_2 , and (surface-gravity sensitive) DDO51 bands
- The measured equivalent width of the Na I doublet at 8190Å combined with the $(V - I)_0$ color of the star.
- The position of the star in an $(I, V - I)$ color magnitude diagram with respect to theoretical RGB isochrones.
- A comparison of the star's photometric vs. spectroscopic metallicity estimates.

¹⁵ <http://astron.berkeley.edu/~cooper/deep/spec2d/primer.html>, <http://astron.berkeley.edu/~cooper/deep/spec1d/primer.html>

The DDO51 diagnostic is only used for field a0, which is the only field in the present work for which DDO51 photometry is available (§ 2.1). The likelihoods for each diagnostic are combined in a weighted average for each star to determine the overall likelihood, $\langle L_i \rangle$, the star is an M31 RGB or MW dwarf star (§ A.1). Based on the overall likelihood, each star is identified as either a secure M31 RGB star ($\langle L_i \rangle > 0.5$, or $> 3 \times$ more likely to be an M31 RGB star than an MW dwarf) or a secure MW dwarf star ($\langle L_i \rangle < -0.5$), or a marginal M31 RGB star ($0 < \langle L_i \rangle < 0.5$) or marginal MW dwarf star ($-0.5 < \langle L_i \rangle < 0$).

An advantage of the diagnostic method for the present analysis is the ability to select a sample that is chosen independently of radial velocity. Since radial velocity is only one of a number of diagnostics which are used to determine the nature of an individual star, the likelihood method (even with the inclusion of the radial velocity diagnostic) presents a significant improvement over the use of velocity cuts to select samples for kinematical analysis by reducing the sensitivity of the sample to velocity. However, by using the likelihood method *without* the radial velocity diagnostic (resulting in overall likelihoods $\langle L_i \rangle_\phi$), we are able to select a sample of M31 red giants that is completely *independent* of the radial velocities of the stars.

Fig. 3 presents the radial velocity distribution of stars selected as M31 red giants based on the diagnostic method with (shaded histograms) and without (thick open histograms) radial velocity included, for multiple $\langle L_i \rangle$ and $\langle L_i \rangle_\phi$ thresholds. For reference, the radial velocity distribution of all stars with successful velocity measurements is also shown (thin open histograms); the MW dwarf star contaminants form the secondary peak centered at $v_{\text{hel}} \approx -50 \text{ km s}^{-1}$. The M31 RGB distributions are similar, with the sample that included the radial velocity diagnostic showing a systematic deficiency of stars at radial velocities near 0 km s^{-1} . The effect of the radial velocity diagnostic on the overall likelihood ($\langle L_i \rangle$ and $\langle L_i \rangle_\phi$) distributions is discussed in § A.1.

The M31 RGB samples identified by their $\langle L_i \rangle$ values (including the radial velocity diagnostic) have a minimal amount of MW dwarf star contamination, but are also kinematically biased against stars with velocities near 0 km s^{-1} (§ A.1). The M31 RGB samples identified by their $\langle L_i \rangle_\phi$ values (not including the radial velocity diagnostic) have a larger amount of dwarf contamination (particularly evident in the bottom panel of Figure 3), but the underlying M31 RGB population is kinematically unbiased.

The RGB sample used in this paper is defined as stars that are designated as secure and marginal M31 red giants by the diagnostic method, with the radial velocity likelihood *not* included in the calculation of a star's overall likelihood of being an M31 RGB star (i.e., $\langle L_i \rangle_\phi > 0$). The number of M31 RGB stars in each field is listed in Table 1. The $\langle L_i \rangle_\phi > 0$ threshold maximizes the completeness of the underlying, *kinematically unbiased* M31 RGB population, but introduces an overall MW dwarf star contamination rate of 5% to the sample (§ A.2). The contamination is largely constrained to $v_{\text{hel}} > -150 \text{ km s}^{-1}$ due to the velocity distribution of MW dwarf stars, and its effect on the measured param-

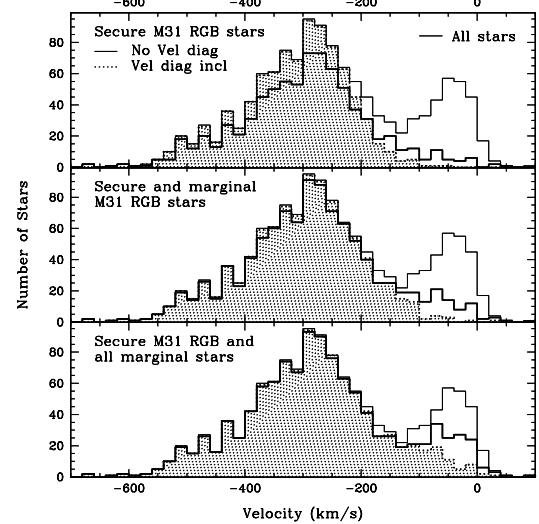


FIG. 3.— The radial velocity distributions of samples with (shaded/dotted histograms) and without (thick open histograms) the radial velocity diagnostic included in the overall likelihood calculation. The radial velocity distribution of all stars with successful radial velocity measurements is shown for comparison (thin open histograms); the MW dwarf star contaminants form the peak at $v_{\text{hel}} \approx -50 \text{ km s}^{-1}$. *Top:* Stars designated as secure ($[\langle L_i \rangle, \langle L_i \rangle_\phi] > 0.5$) M31 red giants only. *Middle:* Stars designated as marginal and secure M31 red giants ($[\langle L_i \rangle, \langle L_i \rangle_\phi] > 0$). *Bottom:* Stars designated as marginal MW dwarfs, marginal M31 red giants, and secure M31 red giants ($[\langle L_i \rangle, \langle L_i \rangle_\phi] > -0.5$). The distributions are similar, but there is a deficiency of stars at velocities near 0 km s^{-1} in the sample that includes radial velocity as a diagnostic.

eters of the M31 RGB sample is quantified in § A.3.

4. STELLAR KINEMATICS IN M31'S SOUTHEAST MINOR-AXIS FIELDS

The data presented in this paper span a range in projected radial distance from the center of M31 of 9 to 30 kpc, along the southeast minor-axis. We refer to this region as the “inner spheroid,” even though it has traditionally been referred to as the “halo” of M31. This region departs from the classical picture of a stellar halo formed from observations of the Milky Way: M31’s inner spheroid is about $10 \times$ more metal-rich than the MW’s halo (Mould & Kristian 1986; Durrell et al. 2004) and follows a de Vaucouleurs $r^{1/4}$ surface density profile (Pritchett & van den Bergh 1994; Durrell et al. 2004), while the halo of the MW follows an r^{-2} power law. In other words, M31’s inner spheroid appears to be a continuation of its central bulge. Recent observations have discovered an outer “pure halo” in M31 which is relatively metal-poor (Kalirai et al. 2006b; Chapman et al. 2006), has a surface density profile that follows an $\sim r^{-2.6}$ power law (Guhathakurta et al. 2005; Irwin et al. 2005), and has been detected out to $R_{\text{proj}} = 165 \text{ kpc}$ (Gilbert et al. 2006).

These observations imply that the spheroid of M31 has two components—an inner, de Vaucouleurs profile spheroid, and an outer, power-law profile halo. We thus use the term *inner spheroid* to distinguish the region $R_{\text{proj}} \sim 9 - 30 \text{ kpc}$ from the canonical central bulge and the newly discovered stellar halo of M31. The

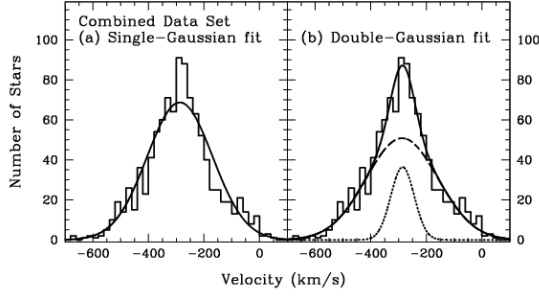


FIG. 4.— The radial velocity distribution of the M31 RGB inner spheroid population. A maximum-likelihood analysis was used to fit an analytic function to the distribution. (a) The best fit single Gaussian has parameters $\langle v \rangle^{\text{sph}} = -287 \text{ km s}^{-1}$ and $\sigma_v^{\text{sph}} = 117 \text{ km s}^{-1}$. A χ^2 test rules out the single-Gaussian fit at a very high confidence level. (b) The best fit double Gaussian (Table 2) is shown as a solid curve, with the narrow component and wide components displayed separately as dotted and dashed curves, respectively.

outer limit of this region is well-defined; a break in the surface brightness profile of M31 RGB stars has been observed at $R_{\text{proj}} \sim 20 - 30 \text{ kpc}$ (Guhathakurta et al. 2005; Irwin et al. 2005), and a crossover between metal-rich and metal-poor components has been observed at $R_{\text{proj}} \sim 30 \text{ kpc}$ (Kalirai et al. 2006b). The inner limit of this region is arbitrary, as the relationship between this component and the central bulge of M31 is not yet clear.

The rest of this section characterizes the line of sight velocity distribution of stars in the inner spheroid of M31 through maximum-likelihood fits of Gaussians to the combined data set (§ 4.1) and to individual fields (§ 4.2). Gaussians provide a convenient means of fitting for multiple kinematical components in the data and characterizing their mean velocity and velocity dispersion. The true shape of the velocity distribution of a structural component in M31 is likely to be different from a pure Gaussian. However, given the limited sample size and the absence of any specific physical model, the choice of Gaussians seems appropriate.

4.1. Maximum-Likelihood Fits to the Velocity Distribution of the Combined Data Set

Figure 4 shows the combined radial velocity distribution of M31 RGB stars from all eight fields along the minor axis, ranging from 9 to 30 kpc in projected radial distance from the center of M31. Fits to the radial velocity distribution were made using a maximum-likelihood technique; the best-fit single (a) and double (b) Gaussians are displayed in Figure 4. A χ^2 analysis rules out the single-Gaussian fit, as the probability is $\ll 1\%$ that the observed radial velocities were drawn from the best-fit distribution. The observed velocity distribution is well fit by a sum of two Gaussians (solid curve, panel b of Fig. 4), composed of a wide Gaussian (dashed curve) centered at $\langle v \rangle^{\text{sph}} = -287.2^{+8.0}_{-7.7} \text{ km s}^{-1}$, with a width of $\sigma_v^{\text{sph}} = 128.9^{+7.7}_{-6.9} \text{ km s}^{-1}$, and a narrow Gaussian (dotted curve), centered at $\langle v \rangle^{\text{sub}} = -285.4^{+12.8}_{-12.4} \text{ km s}^{-1}$ with a width of $\sigma_v^{\text{sub}} = 42.2^{+12.5}_{-14.3} \text{ km s}^{-1}$, which comprises $19^{+9}_{-8}\%$ of the total population (quoted errors represent the 90% confidence limits from the maximum-likelihood analysis). Due to the MW dwarf contaminants in the M31 RGB

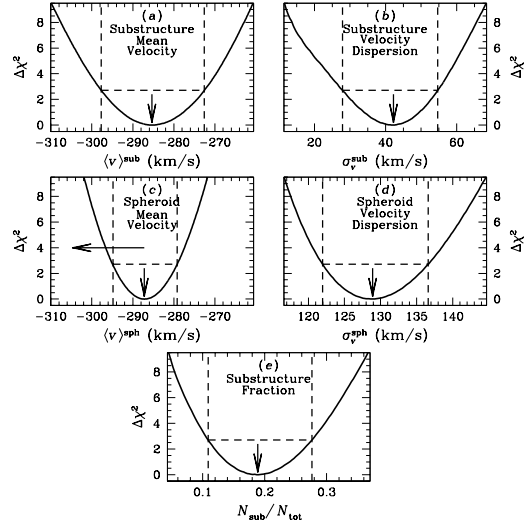


FIG. 5.— Results of the maximum-likelihood analysis for the double-Gaussian fit to the combined M31 RGB inner spheroid sample. The optimal value of each parameter is marked with an arrow, and the 90% confidence limits from the maximum-likelihood analysis are marked with dashed lines. The upper limit of the y-axis represents the 99% confidence limits. The parameter $\Delta\chi^2 \equiv \chi^2 - \chi^2_{\text{min}}$ is plotted as a function of (a) mean velocity of the cold substructure component (narrow Gaussian), $\langle v \rangle^{\text{sub}}$, (b) velocity dispersion of the cold component, σ_v^{sub} , (c) mean velocity of the M31 inner spheroid (wide Gaussian), $\langle v \rangle^{\text{sph}}$, (d) velocity dispersion of the M31 inner spheroid, σ_v^{sph} , and (e) fraction of the total M31 RGB population in the cold component, $N_{\text{sub}}/N_{\text{tot}}$. The horizontal arrow in panel (c) represents the correction to the $\langle v \rangle^{\text{sph}}$ value necessary to offset the bias caused by MW dwarf contamination at $v_{\text{hel}} > -150 \text{ km s}^{-1}$ (§ A.3).

sample used here, the true $\langle v \rangle^{\text{sph}}$ value of the wide Gaussian component is 15 to 20 km s^{-1} more negative than the best-fit value (§ A.3), making it consistent with the systemic velocity of M31 ($v_{\text{sys}} = -300 \text{ km s}^{-1}$). The kinematically hot component corresponds to the inner spheroid of M31 (quantities related to this component are denoted with the subscript “sph”), while the kinematically cold component corresponds to substructure in the inner spheroid (denoted with the subscript “sub”); the discussion of these components and their properties will be deferred to § 5 and § 6, respectively.

Figure 5 shows error estimates from the maximum-likelihood analysis (in the form of $\Delta\chi^2 \equiv \chi^2 - \chi^2_{\text{min}}$ curves) for the five double-Gaussian parameters. The best-fit value of each parameter is marked as well as the 90% confidence limits. The $\Delta\chi^2$ curves have a deep minimum for all five parameters, an indication that the double-Gaussian model is a well-constrained description of the observed radial velocity distribution of inner spheroid stars.

4.2. Maximum-Likelihood Fits to the Velocity Distributions of Individual Fields

The best fit to the combined data set shows evidence of a significant (19%, § 4.1) cold population in these fields. To determine in which fields the cold component is present, we characterize the velocity distributions of each of the individual fields in turn. Figure 6 shows velocity histograms for each of the eight fields.

TABLE 2
RADIAL VELOCITY DISTRIBUTIONS: BEST FIT GAUSSIAN PARAMETERS.

Field	Best fit Gaussian Parameters ^a				Fraction $N_{\text{sub}}/N_{\text{tot}}$
	Cold Component $\langle v \rangle^{\text{sub}}$	σ_v^{sub}	Hot Spheroid ^b $\langle v \rangle^{\text{sph}}$	σ_v^{sph}	
All fields	$-285.4^{+12.8}_{-12.4}$	$42.2^{+12.5}_{-14.3}$	$-287.2^{+8.0}_{-7.7}$	$128.9^{+7.7}_{-6.9}$	$0.19^{+0.09}_{-0.08}$
f109	$-274.5^{+15.4}_{-15.3}$	$120.7^{+11.7}_{-10.1}$...
H11	$-294.3^{+17.3}_{-17.6}$	$55.5^{+15.6}_{-12.7}$	-287.2	128.9	$0.44^{+0.16}_{-0.16}$
f116	$-309.4^{+19.2}_{-17.5}$	$51.2^{+24.4}_{-15.0}$	-287.2	128.9	$0.44^{+0.22}_{-0.17}$
f115	$-270.9^{+18.6}_{-18.6}$	$120.1^{+14.4}_{-12.0}$...
f123	$-279.4^{+5.1}_{-4.6}$	$10.6^{+6.9}_{-5.0}$	-287.2	128.9	$0.31^{+0.11}_{-0.11}$
f135	$-315.1^{+21.3}_{-21.3}$	$127.8^{+16.5}_{-13.6}$...
f130	$-259.8^{+19.3}_{-19.2}$	$131.5^{+14.8}_{-12.5}$...
a0	$-319.2^{+25.2}_{-25.2}$	$131.5^{+29.5}_{-21.6}$...

^a Best-fit Gaussian parameters are determined by a maximum-likelihood analysis. Fields that do not show clear evidence of substructure (§ 4.2) were fit by a single Gaussian. For fields that were fit with a double Gaussian, the wide Gaussian (underlying spheroidal component) parameters were held fixed at the best-fit value for the combined data set (§ 4.2). Errors quoted represent the 90% confidence limits from the maximum-likelihood analysis.

^b The M31 RGB sample used in this analysis was chosen to ensure a high degree of completeness, and thus suffers from some MW dwarf contamination (§ A.2). The MW dwarf star contaminants are largely at $v_{\text{hel}} > -150 \text{ km s}^{-1}$, and cause the best-fit $\langle v \rangle^{\text{sph}}$ values to be biased towards more positive velocities. The true $\langle v \rangle^{\text{sph}}$ values of the M31 RGB population are 15 to 20 km s^{-1} more negative than listed here. The effect on σ_v^{sph} is negligible (§ A.3).

The distribution in each field is first compared to the wide Gaussian component from the double-Gaussian fit to the combined data set (§, 4.1, $\langle v \rangle^{\text{sph}} = -287.2 \text{ km s}^{-1}$, $\sigma_v^{\text{sph}} = 128.9 \text{ km s}^{-1}$) using the reduced χ^2 statistic. Since this component is likely the distribution of the underlying inner spheroid (§ 5), it should be a good fit to the data if a field has a minimal (or no) kinematically cold component. A maximum-likelihood single-Gaussian fit is also performed for each field and compared to the data. Finally, fields which show evidence of substructure are fit by a constrained double Gaussian using the maximum-likelihood technique, with the parameters of the wide Gaussian held fixed at the values found in the double-Gaussian fit to the combined sample. Table 2 summarizes the final fits (single or double-Gaussian) to the velocity distributions in each field.

Field f109: The data in this field are consistent with being drawn from the wide Gaussian component of the double-Gaussian fit in § 4.1. The best-fit single Gaussian to the data in this field has parameters $\langle v \rangle = -274.5 \text{ km s}^{-1}$ and $\sigma = 120.7 \text{ km s}^{-1}$, and the data are also consistent with being drawn from this distribution.

Field H11: The probability the data in this field are drawn from the wide Gaussian component of the double-Gaussian fit in § 4.1 is $P < 1\%$, thus the data are inconsistent with this distribution. drawn from this distribution. The best-fit single Gaussian to the data in this field has parameters $\langle v \rangle = -294.3 \pm 11.6 \text{ km s}^{-1}$ and $\sigma = 106.2^{+8.7}_{-7.7} \text{ km s}^{-1}$, and the data are consistent with being drawn from this distribution. The best-fit value of σ in this field is anomalously low compared to the value of σ_v^{sph} determined from the double-Gaussian fit to the combined data set: the two values are inconsistent at the $\sim 3.5\sigma$ level. This implies that there is a kin-

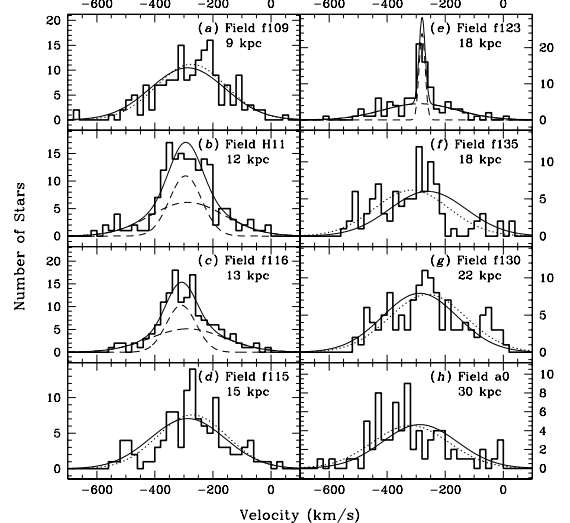


FIG. 6.— Velocity histograms for each of the individual fields with best-fit Gaussians overlaid. Fields that did not show clear evidence of substructure (f109, f115, f130, f135 and a0, § 4.2) are shown with the broad component from the double-Gaussian fit to the full sample (solid curves), as well as the best-fit single Gaussian to the individual field (dotted curves). Fields with substructure were fit with a constrained double Gaussian (H11, f116, f123). For the double-Gaussian fits, both individual Gaussians are shown (dashed curves), scaled to their relative contributions, as well as the combined double-Gaussian fit (solid curves).

atically cold population in this field, and a constrained double-Gaussian fit to this field ($\langle v \rangle^{\text{sub}} = -294.3 \text{ km s}^{-1}$, $\sigma_v^{\text{sub}} = 55.5 \text{ km s}^{-1}$, and $N_{\text{sub}}/N_{\text{tot}} = 0.44$) returns a reduced χ^2 value that is significantly smaller than the reduced χ^2 of the single Gaussian fit.

Field f116: The field is inconsistent with being drawn

from the wide Gaussian component of the double-Gaussian fit in § 4.1 ($P \sim 2\%$). The best-fit single Gaussian to the data in this field has parameters $\langle v \rangle = -292.9_{-11.6}^{+11.5} \text{ km s}^{-1}$ and $\sigma = 97_{-7.5}^{+8.7} \text{ km s}^{-1}$, and the data are consistent with being drawn from this distribution. As in field H11, the best-fit value of σ is inconsistent with σ_v^{sph} from the combined data set, at the $\sim 4.2\sigma$ level. The constrained double-Gaussian fit to this field ($\langle v \rangle^{\text{sub}} = -309.4 \text{ km s}^{-1}$, $\sigma_v^{\text{sub}} = 51.2 \text{ km s}^{-1}$, and $N_{\text{sub}}/N_{\text{tot}} = 0.44$) returns a significantly smaller reduced χ^2 value than that of the single-Gaussian fit.

Field f115: The data in this field are consistent with being drawn from the wide Gaussian component of the double-Gaussian fit in § 4.1. The data in this field are also consistent with being drawn from the best-fit single Gaussian ($\langle v \rangle^{\text{sph}} = -270.9 \text{ km s}^{-1}$ and $\sigma_v^{\text{sph}} = 120.1 \text{ km s}^{-1}$).

Field f123: The probability that the data in this field is drawn from the wide Gaussian component of the double-Gaussian fit in § 4.1 is $P < 1\%$. The probability that the data are drawn from the best-fit single Gaussian ($\langle v \rangle^{\text{sph}} = -270.9 \text{ km s}^{-1}$ and $\sigma_v^{\text{sph}} = 120.1 \text{ km s}^{-1}$) in this field is also $< 1\%$. The data in this field are strongly inconsistent with being drawn from any single Gaussian, but they are consistent with the constrained double-Gaussian fit ($\langle v \rangle^{\text{sub}} = -279.4 \text{ km s}^{-1}$, $\sigma_v^{\text{sub}} = 10.6 \text{ km s}^{-1}$, and $N_{\text{sub}}/N_{\text{tot}} = 0.31$).

Field f135: The data in this field are inconsistent with being drawn from the wide Gaussian component of the double-Gaussian fit in § 4.1 ($P \sim 1\%$). The best-fit single Gaussian to the data in this field has parameters $\langle v \rangle^{\text{sph}} = -315.1 \text{ km s}^{-1}$ and $\sigma_v^{\text{sph}} = 127.8 \text{ km s}^{-1}$, but the data are also inconsistent with being drawn from this distribution ($P \lesssim 1\%$). However, the maximum-likelihood analysis was unable to constrain a double-Gaussian fit to any reasonable degree of certainty—i.e., the error estimates on the parameters show no strong global minima. Field f135 is therefore treated as a field without a definite detection of substructure.

Field f130: The data in this field are inconsistent with being drawn from the wide Gaussian component of the double-Gaussian fit in § 4.1 ($P \lesssim 1\%$), but are consistent with being drawn from the best-fit single Gaussian ($\langle v \rangle^{\text{sph}} = -259.8 \text{ km s}^{-1}$ and $\sigma_v^{\text{sph}} = 131.5 \text{ km s}^{-1}$).

Field a0: The data in this field are inconsistent with being drawn from the wide Gaussian component of the double-Gaussian fit in § 4.1 ($P \sim 2\%$). The best-fit single Gaussian to the data in this field has parameters $\langle v \rangle^{\text{sph}} = -319.2 \text{ km s}^{-1}$ and $\sigma_v^{\text{sph}} = 131.5 \text{ km s}^{-1}$, and the data are consistent with being drawn from this distribution.

We now have a characterization of the kinematical properties of the combined data set and the individual fields. Next, we discuss the trends in the properties of the dynamically hot and cold populations (§ 5 and § 6, respectively), followed by possible physical interpretations of the cold component (§ 7).

5. VELOCITY DISPERSION OF M31'S VIRIALIZED INNER SPHEROID

As discussed in § 4, the radial velocity distribution of the combined data set is inconsistent with a single Gaussian. An analysis of the kinematical profile of the indi-

vidual fields shows that this is due to the presence of a significant amount of substructure (§ 4.2); this substructure produces the kinematically cold component in the double-Gaussian fit to the combined data set. The kinematically hot component in the double Gaussian fit thus represents the underlying virialized inner spheroid of M31. The velocity dispersion of the spheroid based on a maximum-likelihood double Gaussian fit to the combined data set (1013 M31 RGB stars) is $\sigma_v^{\text{sph}} = 128.9 \text{ km s}^{-1}$, as discussed in § 4.

We have combined all of the fields to get a more robust estimate of the velocity dispersion of the inner spheroid, since the individual fields suffer from small number statistics. However, the dynamical quantities ($\langle v \rangle^{\text{sph}}$, σ_v^{sph}) may have radial dependencies. The velocity dispersion of spheroids is expected to decrease with increasing radius (e.g., Navarro et al. 1996, 2004; Mamon & Lokas 2005; Dekel et al. 2005). Since our fields are mostly aligned along the minor axis, we do not expect to see any dependence of $\langle v \rangle^{\text{sph}}$ on radius, unless the rotation axis of the halo is not aligned with that of the disk.

To test for a dependency of the dynamical quantities on radius, we analyze the single Gaussian fits to the velocity distributions in each of the five fields which do not show clear evidence of containing substructure as described in § 4.2 (Table 2 and Fig. 6, dotted curves; the solid curves show the wide Gaussian component from the fit to the full data set). The $\Delta\chi^2$ error estimates for the best-fit Gaussian parameters in these fields are shown in Figure 7. The best-fit $\langle v \rangle^{\text{sph}}$ values in each field are largely consistent with the systemic velocity of M31 ($v_{\text{sys}} = -300 \text{ km s}^{-1}$) once the effect of MW dwarf star contamination is taken into account, with the exception of a0 and f135, whose $\langle v \rangle^{\text{sph}}$ are significantly more negative. Our data show no evidence for a decreasing σ_v^{sph} with increasing radius. However, the fields discussed in this paper only span a range in projected radial distance of $R_{\text{proj}} = 9 - 30 \text{ kpc}$. This is small compared to the size of the total M31 spheroid (inner spheroid and outer halo), which has been shown to extend to 165 kpc (Gilbert et al. 2006). For comparison, Battaglia et al. (2005) use a sample of 240 Galactic halo objects to determine the radial velocity dispersion of the Milky Way halo, and find that it has an almost constant value of 120 km s^{-1} out to 30 kpc, beyond which it decreases with increasing radial distance, declining to 50 km s^{-1} at 120 kpc.

There have been a few previous measurements of the velocity dispersion based on M31 spheroid stars. The closest analog to the present study is Reitzel & Guhathakurta (2002), who fit 80 candidate M31 RGB stars at $R_{\text{proj}} = 19 \text{ kpc}$ on the southeast minor axis with a combination of the Galactic standard model and a wide Gaussian. They found $\sigma_v^{\text{sph}} \sim 150 \text{ km s}^{-1}$ for the M31 velocity dispersion, with the number of M31 RGB stars estimated to be 43% of the population. Guhathakurta et al. (2006) studied a field on the giant southern stream at $R_{\text{proj}} = 33 \text{ kpc}$ and found a velocity dispersion of $\sigma_v^{\text{sph}} = 65_{-21}^{+32} \text{ km s}^{-1}$ for the underlying spheroid based on a sample of ≈ 21 stars. However, if 3 likely RGB stars with $v_{\text{hel}} > -150 \text{ km s}^{-1}$ are included, the estimated velocity dispersion in this field increases to

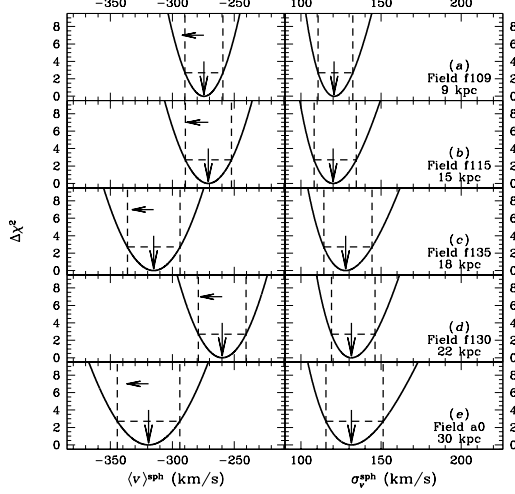


FIG. 7.— Results of the maximum-likelihood analysis for the single-Gaussian fits to individual fields that do not show clear evidence of substructure in the radial velocity distributions (§ 4.2). The panels show $\Delta\chi^2$ for the mean velocity $\langle v \rangle^{\text{sph}}$ (left) and velocity dispersion σ_v^{sph} (right) of M31 RGB stars in fields (a) f109, (b) f115, (c) f135, (d) f130, and (e) a0. As in Figure 5, the optimal values of $\langle v \rangle^{\text{sph}}$ and σ_v^{sph} are marked by arrows, and the 90% confidence limits are shown as dashed lines. The horizontal arrow in each of the left panels represents the correction (magnitude and direction) to the $\langle v \rangle^{\text{sph}}$ value necessary to offset the bias caused by MW dwarf contamination at $v_{\text{hel}} > -150 \text{ km s}^{-1}$ (§ A.3).

$$\sigma_v^{\text{sph}} = 116_{-22}^{+31} \text{ km s}^{-1}.$$

Chapman et al. (2006) has measured a mean velocity dispersion of $\sigma_v^{\text{sph}} = 126 \text{ km s}^{-1}$ for the inner spheroid of M31 using ~ 800 RGB stars in multiple fields surrounding M31. They determine that the spheroid has a central velocity dispersion of 152 km s^{-1} which decreases by $-0.9 \text{ km s}^{-1} \text{kpc}^{-1}$ out to $R_{\text{proj}} \sim 70 \text{ kpc}$. Many of their fields are near M31's major axis and have significant contamination from the extended rotating component identified as the extended disk in Ibata et al. (2005). They isolate a sample of M31 spheroid stars by removing all stars within 160 km s^{-1} of the measured disk velocity in each field, and by removing all stars with $v_{\text{hel}} > -160 \text{ km s}^{-1}$ (MW dwarf star contaminants). This “windowing” technique leaves them with a sample of M31 spheroid stars that is significantly incomplete, but is largely uncontaminated by M31's extended disk or MW dwarf stars. Based on the Chapman et al. (2006) result, we would expect to measure a velocity dispersion of 146 km s^{-1} in our innermost field, f109, which would decrease to a velocity dispersion of 125 km s^{-1} in our outermost field, a0. The predicted velocity dispersion of 146 km s^{-1} in field f109 exceeds the 90% confidence limits of the maximum-likelihood fit and is just within the 99% confidence limit, and the data presented in this paper show no evidence of a strong trend in σ_v^{sph} with radius.

The previous measurements of the stellar velocity dispersion of the M31 spheroid relied either on samples that were chosen on the basis of radial velocity cuts or on a statistical fit to the combined M31 RGB and MW dwarf populations. Our measurement of the velocity disper-

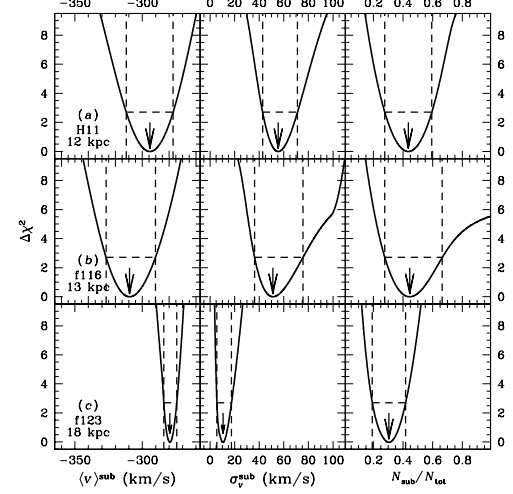


FIG. 8.— Results of the maximum-likelihood analysis for the narrow Gaussian parameters from the double-Gaussian fits to fields (a) H11, (b) f116, and (c) f123. The panels show $\Delta\chi^2$ as a function of (left) mean velocity $\langle v \rangle^{\text{sub}}$, (middle) velocity dispersion σ_v^{sub} , and (right) fraction of stars in the cold component, $N_{\text{sub}}/N_{\text{tot}}$. The parameters of the wide Gaussian component in these fits have been fixed at the best-fit values from the double-Gaussian fit to the combined M31 RGB sample (§ 4). As in Figure 5, the optimal values of each parameter are marked by arrows, and the 90% confidence limits are shown as dashed lines. The velocity dispersion decreases with increasing radial distance from the center of M31.

sion of M31's spheroid is unique in that it is based on a sample of spectroscopically confirmed M31 RGB stars that were chosen *without* the use of radial velocity (§ 3). Our method also allows us to quantify and correct for the effect of MW dwarf star contamination (§§ A.2–A.3).

6. PROPERTIES OF THE MINOR-AXIS SUBSTRUCTURE

6.1. Spatial Trends

As discussed in § 4.2, fields H11, f116, and f123 show evidence of a cold component in their radial velocity distributions (Fig. 6), and were fit by a sum of two Gaussians with the wide Gaussian parameters held fixed (Table 2). The $\Delta\chi^2$ error estimates for the free parameters ($\langle v \rangle^{\text{sub}}$, σ_v^{sub} , and $N_{\text{sub}}/N_{\text{tot}}$) are shown in Figure 8 for each field.

If the three fields are considered together, a pattern emerges. Both the velocity dispersion and the fraction of stars in the cold component decrease with increasing radial distance. The substructure in fields H11 and f116 (at $R_{\text{proj}} = 12$ and 13 kpc , respectively) is significantly wider than the substructure in field f123 ($R_{\text{proj}} = 18 \text{ kpc}$). The substructure also appears to be more dominant in fields H11 and f116 than in field f123.

Figure 9 presents the velocities of the M31 RGB stars as a function of their distance along the major and minor axes of M31. The cold component can be seen as a triangular-shaped feature that narrows to a sharp point as the distance along the minor axis increases. The fields that overlap the triangular-shaped feature in minor axis distance are (in order of increasing distance along the minor axis) H11, f116, f115, f135, and f123. Stars in fields H11, f116 and f123 that are within the area denoted by

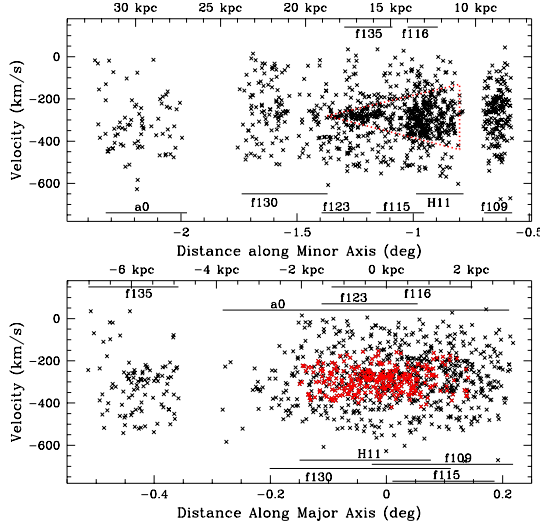


FIG. 9.— Distribution of RGB stars in velocity vs. distance along the minor (top) and major (bottom) axes of M31. The range of minor (major) axis distances of stars in each field are shown in the top (bottom) panel. *Top:* The cold component is visible as a triangular feature that starts at -0.8° (10.9 kpc) and narrows to a point at -1.35° (18.4 kpc) along the minor axis. This feature is outlined in red (dotted line). *Bottom:* Stars in fields H11, f116, and f123 that fall within the triangular outline in the top panel are colored red. In the fields in which the substructure is present, the cold component is spread evenly as a function of projected distance from the minor axis.

the dotted line are shown as red crosses in the bottom panel. In the fields in which it is observed, the cold component is spread evenly along the direction of the major axis, and is centered at $v_{\text{hel}} \sim -285 \text{ km s}^{-1}$. The majority of the fields overlap in position along the major axis; the exception is field f135, which is the isolated set of points at large major axis distances (-0.51° to -0.36° , or -7.0 kpc to -4.9 kpc) in the bottom panel of Figure 9. Field f123 extends from -1.18° to -1.39° (16.1 kpc to 19.0 kpc) along the minor axis; the tip of the feature is seen in this field. This field also has the coldest substructure in the radial velocity histograms (Fig. 6, Table 2). Field H11 brackets the other edge of the feature along the minor axis. Field H11 has a range in minor axis distance of -0.78° to -0.99° (10.7 kpc to 13.5 kpc), and has a large degree of overlap with field f116 in both their minor and major axis distance ranges. The fits to the cold component in these two fields return similar σ_v^{sub} and $N_{\text{sub}}/N_{\text{tot}}$ estimates (Table 2).

Of the fields in which substructure was not clearly detected kinematically (§ 4.2), fields f135 and f115 are both within the minor-axis distance range spanned by the observed substructure. A two-sided Kolmogorov-Smirnov (KS) test finds that the radial velocity distribution of field f115 is consistent with the radial velocity distribution of its closest neighbor, field f116 (Fig. 2). It is, however, inconsistent with the best-fit double Gaussian to field f116. Although the radial velocity distribution of field f135 is not well-fit by a double Gaussian (§ 4.2), there is a concentration of stars near $v_{\text{hel}} \sim -300 \text{ km s}^{-1}$ in its radial velocity distribution (Fig. 6). We will discuss these fields further in the context of the physical interpretation of the substructure (§ 7.1). Fields f130 and a0 are at larger minor axis distances than the tip of the fea-

ture, and field f109 is interior to the feature. The fact that substructure is not detected in these fields is consistent with our favored physical interpretation of the substructure, which will be discussed in § 7.1.

6.2. Metallicity Distribution

So far we have considered only the kinematic properties of the minor-axis population. The distribution of stellar metallicities, however, is also a powerful diagnostic of the presence and origin of substructure, since different galactic components (e.g., disk, inner spheroid) and tidal debris all have different formation histories, and therefore different chemical abundances.

Figure 10 (a) displays the $[\text{Fe}/\text{H}]$ vs. v_{hel} distribution for the M31 RGB stars. The $[\text{Fe}/\text{H}]$ values are based on a comparison of the star's position within the $(I, V - I)$ CMD to a finely spaced grid of theoretical 12 Gyr, $[\alpha/\text{Fe}] = 0$ stellar isochrones (Kalirai et al. 2006b; Vandenberg et al. 2006) adjusted to the distance of M31 (783 kpc; Stanek & Garnavich 1998; Holland 1998). Stars with $[\text{Fe}/\text{H}] < -1$ appear evenly distributed in velocity, while there is an obvious clump of metal-rich stars with velocities near -300 km s^{-1} . The bottom panels (b-d) show velocity histograms for stars in three $[\text{Fe}/\text{H}]$ bins: (b) $[\text{Fe}/\text{H}] \geq -0.5$, (c) $-1.0 < [\text{Fe}/\text{H}] < -0.5$, and (d) $[\text{Fe}/\text{H}] \leq -1.0$. The strength of the cold component in each metallicity bin is measured by performing a maximum-likelihood double-Gaussian fit to the velocity distribution. Only the fraction of stars in the cold component ($N_{\text{sub}}/N_{\text{tot}}$) is allowed to vary; the rest of the parameters are held fixed at the best-fit values from the fit to the full M31 RGB sample (Table 2). The fraction of stars in the cold component is 29.2% in (b), 20.9% in (c), and is negligible in (d), indicating that the substructure is metal-rich.

Figure 11 compares the metallicity distributions of stars in the velocity range of the cold substructure (*solid line*) discovered in fields H11, f116, and f123 and stars that are identified with the hot spheroidal component (*dashed line*) in those fields. The hot spheroidal distribution (v_{outer}) is based on stars whose velocities are greater than $\pm 2 \times \sigma_v^{\text{sub}}$ away from $\langle v \rangle^{\text{sub}}$. This minimizes contamination of the spheroidal component by stars associated with the substructure. An additional constraint on the v_{outer} distribution is that only stars with $v_{\text{hel}} < -150 \text{ km s}^{-1}$ are included; the sample has a high MW dwarf contamination rate for $v_{\text{hel}} > -150 \text{ km s}^{-1}$ (§ A.2). Stars within the velocity range of the cold component can only statistically be identified as belonging to the hot spheroid or cold component, thus it is not possible to identify an uncontaminated substructure sample. Stars with velocities within $\pm 1 \sigma_v^{\text{sub}}$ of $\langle v \rangle^{\text{sub}}$ are used for the v_{inner} $[\text{Fe}/\text{H}]$ distribution, in order to maximize the number of substructure stars while minimizing the contribution of spheroid stars.

The $[\text{Fe}/\text{H}]$ distribution of the v_{outer} sample is more metal-poor, with a peak at lower $[\text{Fe}/\text{H}]$ values and a larger metal-poor tail than the $[\text{Fe}/\text{H}]$ distribution of the v_{inner} sample. The mean and median metallicity of the v_{outer} sample are $\langle [\text{Fe}/\text{H}] \rangle_{\text{mean}} = -0.72$ and $\langle [\text{Fe}/\text{H}] \rangle_{\text{med}} = -0.63$, while the mean and median metallicity of the v_{inner} sample are $\langle [\text{Fe}/\text{H}] \rangle_{\text{mean}} = -0.55$ and $\langle [\text{Fe}/\text{H}] \rangle_{\text{med}} = -0.49$. A KS test returns a probability of 0.7% that the two distributions are drawn from the same

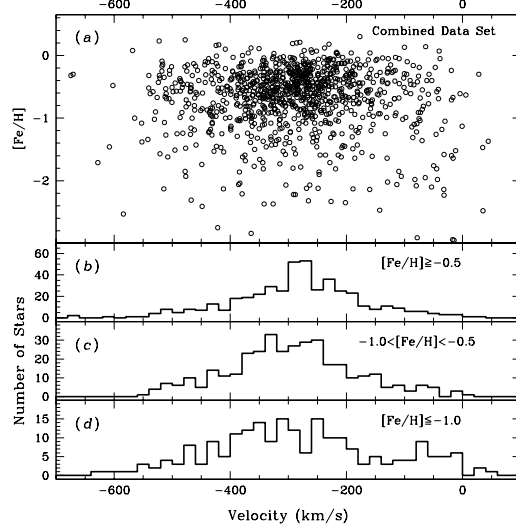


FIG. 10.— (a) Metallicity vs. heliocentric velocity for the full M31 RGB sample. The majority of the population is metal-rich, with an evenly distributed metal-poor tail over the full range of velocities. A concentration of metal-rich stars near $v_{\text{hel}} = -300 \text{ km s}^{-1}$ can be seen. The bottom three panels show velocity histograms for subsets of the data: (b) $[\text{Fe}/\text{H}] \geq -0.5$, (b) $-1.0 < [\text{Fe}/\text{H}] < -0.5$, and (d) $[\text{Fe}/\text{H}] \leq -1.0$. The cold component is more dominant in the metal-rich samples. A maximum-likelihood double-Gaussian fit was performed for each subset of the data, with all of the parameters except $N_{\text{sub}}/N_{\text{tot}}$ held fixed at the best-fit values for the complete M31 RGB sample (§ 4.1, Fig. 4, Table 2). The cold component comprises a negligible fraction of the population in (d), 20.9% of the population in (c), and 29.2% of the population in (b), indicating that the cold component is metal-rich.

parent distribution. The v_{inner} distribution is highly contaminated by spheroid stars even within $\pm 1\sigma_v^{\text{sub}}$ of $\langle v \rangle^{\text{sub}}$ (Fig. 6); the estimated contamination of the v_{inner} sample by spheroid stars is 32.5%. A statistical subtraction of the v_{outer} distribution (scaled by the contamination rate) from the v_{inner} distribution yields a distribution with a mean and median metallicity of $\langle [\text{Fe}/\text{H}] \rangle_{\text{mean}} = -0.52$ and $\langle [\text{Fe}/\text{H}] \rangle_{\text{med}} = -0.45$.

A further effect on the measured metallicity difference is the assumed age of the population. Varying the age between 6 and 14 Gyr introduces an ≈ 0.4 dex spread in the $[\text{Fe}/\text{H}]$ values derived from the isochrone fitting. If the stars associated with the substructure are younger than the assumed 12 Gyr (a reasonable assumption for the spheroid stars), the $[\text{Fe}/\text{H}]$ values shown here will be biased towards low metallicities, and thus the intrinsic difference in metallicity between the two populations will be greater. We have also assumed that all stars are at the same line-of-sight distance as M31's center. This is a valid approximation for the inner spheroid: at $R_{\text{proj}} = 20 \text{ kpc}$, the spread in line-of-sight distances is expected to be about $\pm 20 \text{ kpc}$ (a spread in apparent magnitude of ± 0.05 dex), which corresponds to a spread in $[\text{Fe}/\text{H}]$ of approximately ± 0.03 dex. If the substructure is systematically more (less) distant than M31's spheroid (§ 7.1), the intrinsic difference in metallicity between the populations will be slightly smaller (greater).

Although fields f115 and f135 do not show clear evidence of a cold component (§ 4.2), they are both within the minor-axis range of the substructure (§ 6.1). If the cold components in fields H11, f116, and f123 have the

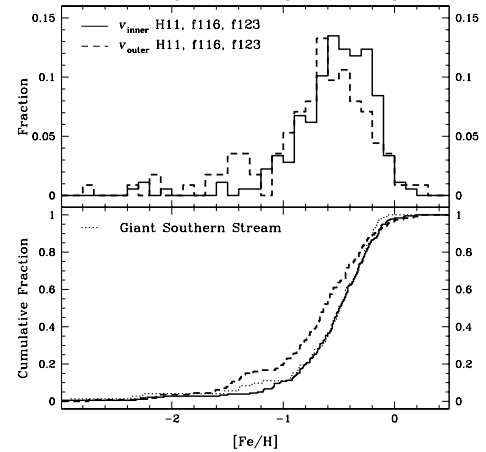


FIG. 11.— The $[\text{Fe}/\text{H}]$ distribution of the v_{inner} (solid line) and v_{outer} (dashed line) components in fields H11, f116, and f123, in histogram (top) and cumulative (bottom) form. The v_{inner} (cold component) sample is defined to be stars with velocities within the range $\langle v \rangle^{\text{sub}} - \sigma_v^{\text{sub}} < v_{\text{hel}} < \langle v \rangle^{\text{sub}} + \sigma_v^{\text{sub}}$, where $\langle v \rangle^{\text{sub}}$ and σ_v^{sub} represent the best-fit narrow Gaussian components in each field. This range was chosen to maximize the percentage of substructure stars compared to hot spheroidal stars. The v_{outer} (hot spheroid) sample consists of stars with velocities $v_{\text{hel}} < \langle v \rangle^{\text{sub}} - 2\sigma_v^{\text{sub}}$ or $\langle v \rangle^{\text{sub}} + 2\sigma_v^{\text{sub}} < v_{\text{hel}} < -150 \text{ km s}^{-1}$. This minimizes contamination from substructure stars and MW dwarf stars (§ A.2) in the hot spheroidal $[\text{Fe}/\text{H}]$ distribution. The v_{inner} sample is slightly more metal rich than the v_{outer} sample. Since the v_{inner} sample is contaminated by spheroid stars, the true difference in $[\text{Fe}/\text{H}]$ between the substructure and spheroid populations is somewhat greater than indicated in this plot. The cumulative $[\text{Fe}/\text{H}]$ distribution of stars in M31's GSS (from fields at 33 and 21 kpc; Guhathakurta et al. 2006; Kalirai et al. 2006a) is plotted in the bottom panel for comparison (thin dotted line), and will be discussed in § 7.1.

same physical origin, it is reasonable to postulate that there may be substructure in fields f115 and f135 that is not detected by the fits to the radial velocity distributions. The stars in fields f115 and f135 that fall within the triangular region marked in Figure 9 have average $[\text{Fe}/\text{H}]$ values of -0.67 and -0.56 ($\langle [\text{Fe}/\text{H}] \rangle_{\text{median}} = -0.57$ and $\langle [\text{Fe}/\text{H}] \rangle_{\text{median}} = -0.46$), respectively, and stars from these fields that have velocities both outside the triangular region and $v_{\text{hel}} < -150 \text{ km s}^{-1}$ have average $[\text{Fe}/\text{H}]$ values of -0.73 and -0.76 ($\langle [\text{Fe}/\text{H}] \rangle_{\text{median}} = -0.81$ and $\langle [\text{Fe}/\text{H}] \rangle_{\text{median}} = -0.61$), respectively. The $[\text{Fe}/\text{H}]$ distributions of stars in fields f135 and f115 that are within the triangular region of the substructure are consistent with both the v_{inner} and v_{outer} distributions. The difference between the substructure and spheroid metallicity distributions is small, and is only statistically significant when the three substructure fields are combined (into the v_{inner} and v_{outer} samples). The number of stars within a restricted velocity range in any given field is too small to support a statistically significant comparison.

7. PHYSICAL ORIGIN OF THE COLD COMPONENT

The observed M31 RGB population along the southeast minor-axis exhibits a spatially varying kinematically cold component, which has a higher mean metallicity than the underlying inner spheroid population. A cold component with these properties could be part of the out-

skirts of M31's disrupted disk or debris left by disrupted satellites. The models of F07 predict debris stripped from the progenitor of the GSS should be present in these fields. (It is also possible, of course, that the observed substructure is satellite debris *unrelated* to the GSS.) This section examines both the continuation of the GSS (§ 7.1) and M31's disturbed disk (§ 7.2) as possible physical origins of the cold component.

7.1. Relation to the Giant Southern Stream

7.1.1. Model of a Recent Interaction

Debris in the form of coherent shells has been observed in many elliptical galaxies; these shells are believed to be formed by the tidal disruption of a satellite galaxy on a nearly radial orbit (e.g., Schweizer 1980; Hernquist & Quinn 1988; Barnes & Hernquist 1992). F07 presents the hypothesis that the northeast and western “shelves” observed in M31 (Figs. 1 and 12, also see Fig. 1 of F07) are a similar phenomenon to these shell systems, and have been created by the disruption of the progenitor of the GSS. Shells have coherent velocities, and display a distinctive triangular shape in the v_{los} vs. R_{proj} plane (Merrifield & Kuijken 1998, F07). In general, as R_{proj} approaches the boundary of the shell the spread in velocities approaches zero, with the mean velocity at the tip of the triangle expected to be at the systemic velocity of the system.

F07 present an N -body simulation of an accreting dwarf satellite within M31's potential (Fig. 12). The simulations use a static bulge+disk+halo model which is based on the M31 mass models in Geehan et al. (2006) combined with the observed stellar density distribution in the halo (Guhathakurta et al. 2005), and assumes an isotropic velocity distribution in the outer halo. The simulated satellite's physical and orbital properties have been chosen to reproduce the observed properties of the GSS and northeast shelf, using the methods of Fardal et al. (2006). The simulations show that the orbit which reproduces these features also reproduces a photometric feature identified in F07 as the “western shelf” and an observed stream of counter-rotating planetary nebulae (Merrett et al. 2003, 2006).

Figure 12 shows the projected sky positions (in M31-centric coordinates) of the satellite particles from the F07 simulation. The particles are color-coded by shell, or equivalently, by the number of pericentric passages they have made. Green particles represent particles approaching their first pericentric passage; they correspond to the observed GSS. Red particles correspond to the observed northeast shelf; they are between their first and second pericentric passages. Magenta particles represent the western shelf identified in F07, and are between their second and third pericentric passages. The blue particles are between their third and fourth pericentric passages, and represent the “southeast shelf” predicted by F07. This last feature is predicted to extend out to a radius of 18 kpc and is expected to be very faint, as it consists of particles further forward in the continuation of the stream than the more visible northeastern and western shelves. This feature actually covers $\sim 180^\circ$ in position angle on the east side of M31, although it is likely to only be visible in the southeast due to its overlap with the northeast shelf and M31's disk. In the F07 simula-

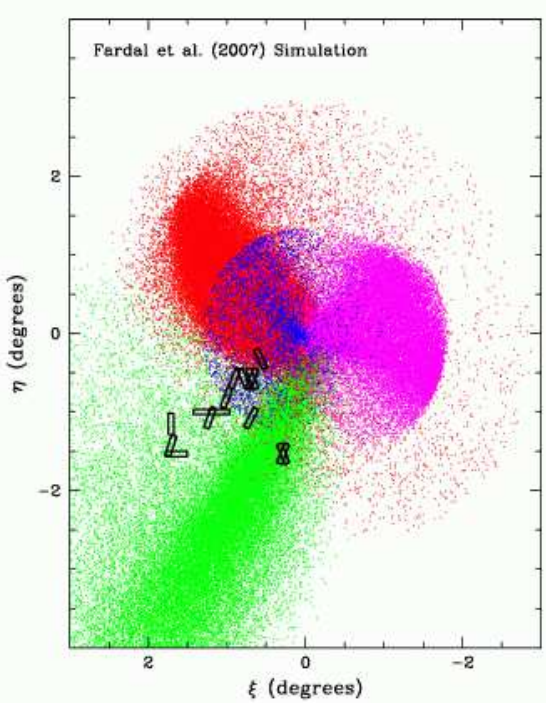


FIG. 12.— Projected sky position (in M31 centric coordinates ξ and η) of tidal debris in the F07 simulations of the merger of a dwarf galaxy with M31. Particles approaching their first pericentric passage are part of the GSS (green). Particles approaching their second pericentric passage form the northeast shelf (red), and particles approaching their third pericentric passage form the Western shelf (magenta) identified in F07. Particles in blue are approaching their fourth pericentric passage, and form a faint shelf feature which is predicted to be most easily visible in the southeast. The position of our spectroscopic masks are also shown; fields f123 and f135 straddle the edge of the southeast shelf (Fig. 2). The two masks at $\xi = 0.3^\circ$, $\eta = -1.5^\circ$ are in field H13s, which is discussed in § 7.1.3 and § 8.

tions, the northeast shelf is made up of both the leading material from the progenitor's first pericentric passage and trailing material from its second pericentric passage, while the western shelf is formed by leading material. The simulations are unable to constrain whether or not the satellite disrupts completely, as this is dependent on the central density of the satellite.

Figure 13 presents the distribution of particles from the F07 simulation in the v_{los} vs. minor-axis distance plane. The figure shows particles related to the merging satellite as well as particles associated with the static bulge+disk+stellar-halo M31 model used in F07. In order to carry out a precise comparison to our observational data set, the F07 simulation particles were selected based on their projected sky position; all particles that fall inside a $16' \times 10'$ area (the approximate area of one DEIMOS mask is $16' \times 4'$) centered on the position of our observed fields, and oriented at the position angle of our observed masks, are displayed in the top panel. The bottom panel shows the same particles, but with the satellite particles color-coded by shell (or, equivalently, the number of orbits they have made) as in Figure 12. Green particles are associated with the GSS and red particles with the northeast shelf. The blue particles, which are part of the predicted “southeast” shelf, form the distinctive triangular shape expected of a shell feature in the

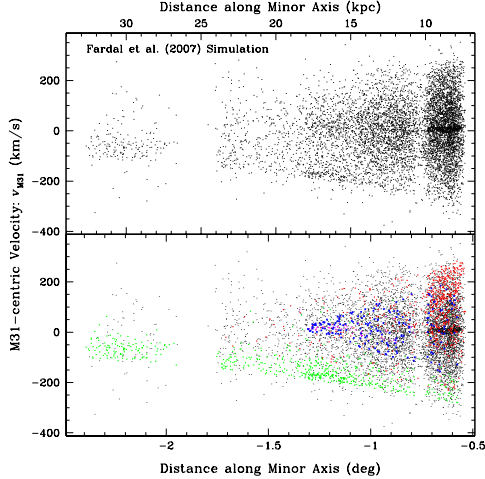


FIG. 13.— Line of sight velocity (M31-centric) vs. minor-axis distance for particles from the F07 simulations of the orbit of the progenitor of the GSS. *Top:* Particles (substructure plus the static bulge+disk+stellar-halo of M31) in the region of M31 covered by each of our DEIMOS masks. The area from which particles have been drawn has been increased relative to the size of a slitmask to increase the number of particles. The obvious cold concentration of stars at $v_{M31} \approx 0 \text{ km s}^{-1}$ extending in minor axis distance from -0.7° to -0.5° (9.6 to 6.8 kpc) corresponds to the disk of M31. No signature of a smooth disk is seen in our data. *Bottom:* The satellite particles are color-coded according to which shell they are in: the giant southern stream (green), the northeast shelf (red), and the predicted southeast shelf (blue). Black points are particles from the bulge+disk+stellar-halo of M31. The blue particles form a tight triangular shape, with an increasingly wide kinematic profile as the minor axis distance to the center of M31 decreases, as is seen in the corresponding data plot (Fig. 9). The tip of the triangle at -1.35° (18.4 kpc) in the simulated data agrees well with the observed tip in the data in field f123.

$R_{\text{proj}}\text{-}v_{\text{los}}$ plane. (Since most of our fields are on/near M31's minor-axis, minor-axis distance is a good proxy for R_{proj} .)

7.1.2. Comparison of Model to Data

Sky Position: Figure 12 shows the projected sky positions (in M31-centric coordinates) of the satellite particles from the F07 simulation as well as the size, position and orientation of our Keck/DEIMOS slitmasks (*rectangles*). Fields f123 and f135 land on the edge of the predicted southeast shelf (*blue particles*), while fields f115, f116, H11 and f109 all lie within the boundary of the southeast shelf and fields f130 and a0 lie beyond it. Thus, the edge of the predicted shell feature passes directly through our CFHT/MegaCam image. There is an apparent edge visible in the CFHT starcount map (Fig. 2), in the same location as that predicted for the southeast shelf (the observed edge passes through field f123). A close inspection of the Ibata et al. (2005) starcount map (Fig. 1) reveals a point of bifurcation between the edge of the northeast shelf and a fainter feature at $\xi \approx 1.6^\circ$, $\eta \approx 0.2^\circ$, in rough agreement with the bifurcation of the two features in Figure 12. This bifurcation is more evident in the Sobel-filtered map in F07 (their Fig. 1). The radii of the shells in the simulation is robust (§ 4.2 of F07); thus the agreement between the observations and the simulations is a strong confirmation of the validity of the F07 model.

Kinematic Trends: The substructure observed in our

minor-axis fields shows the distinctive triangular velocity pattern expected of a shell feature in the $R_{\text{proj}}\text{-}v_{\text{los}}$ plane and seen in the distribution of the particles from the southeast shelf. The distribution of velocities narrows to a tip at a minor axis distance of $\approx -1.35^\circ$ (18.4 kpc) in the simulated particle distribution (Fig. 13), which is similar to the position of the tip of the velocity distribution in our observed data (Fig. 9). At a minor-axis distance of -1° (13.7 kpc), the velocity distribution of the observed substructure has widened to a spread of $\sim 200 \text{ km s}^{-1}$ (measured from the edges of the feature), also in agreement with the velocity spread of the predicted southeast shelf.

The “boxy” shape of the radial velocity distribution in field H11 (Fig. 6) is also consistent with the interpretation of the substructure being part of a shell system. The velocity distributions of shells have a clearly defined minimum and maximum radial velocity at a given R_{proj} , and stars tend to congregate at the minimum and maximum velocities (Merrifield & Kuijken 1998, F07), though their location in the $R_{\text{proj}}\text{-}v_{\text{los}}$ plane depends on the region they occupy in space (cf. the discussion in F07).

A maximum-likelihood Gaussian fit to the particles identified with the southeast shelf and within the minor axis distance spanned by field f123 yields parameters of $\langle v \rangle = -280.6 \text{ km s}^{-1}$ and $\sigma_v = 19.4 \text{ km s}^{-1}$. A Gaussian fit to the southeast shelf particles within the minor axis range spanned by fields f116 and H11 returns $\langle v \rangle = -292.6 \text{ km s}^{-1}$ and $\sigma_v = 60.5 \text{ km s}^{-1}$. The mean velocity and dispersion of the predicted shelf is in good agreement with the properties of the observed substructure (Table 2).

Metallicity Distribution: If the substructure identified in this paper is part of the predicted southeast shelf in F07, it should have a similar metallicity distribution to that of the GSS, since the two structures originated from the same progenitor. As part of our Keck/DEIMOS survey of M31's inner spheroid and halo, we have taken spectra in two fields located on the GSS: a field at $R_{\text{proj}} = 33 \text{ kpc}$ (Guhathakurta et al. 2006) and a field at $R_{\text{proj}} = 21 \text{ kpc}$ (H13s; Kalirai et al. 2006a). The cumulative [Fe/H] distribution of stars identified kinematically as belonging to the GSS in these two fields is plotted in the bottom panel of Figure 11 (thin dotted line). It is very similar to the [Fe/H] distribution of stars that are kinematically associated with the substructure in fields H11, f116, and f123. The mean and median metallicity of the GSS stars shown here are $[\text{Fe}/\text{H}]_{\text{mean}} = -0.62$ and $[\text{Fe}/\text{H}]_{\text{med}} = -0.50$. The estimated number of inner spheroid star contaminants in the GSS sample is a few stars (Guhathakurta et al. 2006; Kalirai et al. 2006a). If the 3 most metal-poor stars are removed ($[\text{Fe}/\text{H}] < -2.25$), the mean and median metallicity increases to $[\text{Fe}/\text{H}]_{\text{mean}} = -0.53$ and $[\text{Fe}/\text{H}]_{\text{med}} = -0.46$. In comparison, the estimated metallicity in the substructure presented here (corrected for spheroid contamination) is $[\text{Fe}/\text{H}]_{\text{mean}} = -0.52$ and $[\text{Fe}/\text{H}]_{\text{med}} = -0.45$ (§ 6.2). The [Fe/H] values of the GSS stars have not been corrected for the GSS' measured distance relative to M31 ($\sim 50 \text{ kpc}$ behind M31 for these 2 fields; McConnachie et al. 2003). Accounting for this effect would decrease the average metallicity of the GSS by $\sim 0.1 \text{ dex}$. The distance to the substructure is not known, although the F07 simulations

predict that the southeast shelf should be approximately at M31’s distance, with a spread in distances of ± 9.2 kpc (this corresponds to $\pm 2\sigma$ in terms of the distribution of particle distances).

Strength of the Cold Component: The cold component comprises 44% of the total population of observed stars in fields H11 and f116 and 31% of observed M31 RGB stars in field f123 (Table 2). This corresponds to a lower limit for the total fraction of stars in the cold component of 21.7% in the fields within the predicted range of the southeast shelf (f109, H11, f116, f115, f123, and f135). The southeast shelf in the simulations is much weaker, comprising only 2.7% of the total population in these fields (this number increases to 3.4% if the number of shelf particles is compared only to the number of bulge+disk+stellar-halo M31 particles). The strength of the feature in the simulations is highly dependent on the mass of the progenitor and the time since the first collision (F07). Thus, the strength of the observed substructure will place interesting constraints on future models of the stream, but cannot be used as a reliable discriminant of the applicability of the model at the present time.

Fields Without Clear Detection of Substructure: We do not find a clear detection of substructure in fields f130 and a0. In the context of the southeastern shelf, this is not surprising as both these fields are beyond the radial range spanned by the shelf (Fig. 12). Field f109 is significantly inward of the innermost field in which we detect substructure. In the simulation, the particles associated with the southeast shelf continue into the region covered by field f109 with a spread in velocities of ~ 350 km s $^{-1}$ (Fig. 13). The data in field f109 is consistent with being drawn from a single Gaussian (§ 4.2) and shows no evidence of substructure. A secondary component with a spread in velocities as wide as predicted would be very difficult to differentiate from the broad spheroidal component, and would require a much larger sample of M31 RGB stars in this field than is currently available.

Field f115 is well within the boundaries of the southeast shelf. As discussed in § 6.1, its velocity distribution is consistent with being drawn from the same parent distribution as field f116. The shell in field f115 may be difficult to detect in our data due to the broad (~ 55 km s $^{-1}$) nature of the substructure and the smaller number of stars available in this field ($\sim 50\%$ less than in field f116), or the shelf may be inherently clumpy.

Field f135 is on the edge of the simulated shelf, and does show evidence for a peak of stars near $v_{\text{hel}} \sim -300$ km s $^{-1}$ in its radial velocity histogram. In light of the simulations, we discuss this field in detail in the next section.

7.1.3. Interpretation of Field f135: Multiple Components

Field f135 is in the minor axis distance range spanned by the substructure, and shows evidence of a metal-rich population (§ 6.2). The $\langle v \rangle^{\text{sph}}$ value from the best fit single Gaussian to the velocity distribution in this field is significantly more negative than the $\langle v \rangle^{\text{sph}}$ value from the double-Gaussian fit to the combined data set (§ 4.2, Figs. 6 and 7). In addition, field f135 is inconsistent with being drawn from a single Gaussian and is also not well-fit by a double Gaussian.

The F07 simulations predict that, in addition to the southeast shelf (*blue particles*, Figs. 12 and 13), some debris from the GSS should be present in field f135 (*green particles*, Figs. 12 and 13). The sky coordinates of field f135 are $\xi = 0.7$, $\eta = -1.1$, which places it on the edge of both the GSS and the southeast shelf in Figure 12. Motivated by the close match between the observations and simulations of substructure in fields H11, f116 and f123, we carry out a constrained fit of the radial velocity histogram of field f135 to the sum of three Gaussians.

The mean velocity and velocity dispersion of F07’s simulated southeast shelf and GSS particles in field f135 are $\langle v \rangle^{\text{SE}} = -286$ km s $^{-1}$, $\sigma_v^{\text{SE}} = 19$ km s $^{-1}$ and $\langle v \rangle^{\text{GSS}} = -458$ km s $^{-1}$, $\sigma_v^{\text{GSS}} = 40$ km s $^{-1}$. These values were used as rough constraints for the triple Gaussian fit: the means were allowed to vary within ± 100 km s $^{-1}$ of the predicted values and the dispersions were allowed to vary from 1 km s $^{-1}$ to $3 \times \sigma_v^{\text{SE}}$ and $2 \times \sigma_v^{\text{GSS}}$. The wide Gaussian component was held fixed at the best-fit value for the wide component in the combined data set: $\langle v \rangle^{\text{sph}} = -287.2$ km s $^{-1}$ and $\sigma_v^{\text{sph}} = 128.9$ km s $^{-1}$ (§ 4.1). The maximum-likelihood triple Gaussian fit is displayed in Figure 14 (*solid curve*). The wide underlying inner spheroid component (*dot-dashed curve*) comprises 45% of the population. The “southeast shelf” component (*dashed curve*), which is the narrow peak at $\langle v \rangle^{\text{sub}} = -273$ km s $^{-1}$, comprises 30% of the population and has a width of $\sigma_v^{\text{sub}} = 30$ km s $^{-1}$. The “GSS” component (*dotted curve*) at $\langle v \rangle = -449$ km s $^{-1}$ has a dispersion of $\sigma_v = 55$ km s $^{-1}$ and comprises 25% of the total population. If instead a more constrained fit is carried out with the $\langle v \rangle$ and σ_v parameters for all three Gaussian components held fixed (at the predicted values for the simulated shelf and stream particles and at the best-fit values for the inner spheroid component of the combined data set) and only the fractions of stars in the various components are allowed to vary, the best-fit distribution has $N_{\text{shelf}}/N_{\text{tot}} = 0.18$ and $N_{\text{GSS}}/N_{\text{tot}} = 0.17$.

The velocity dispersion of $\sigma_v = 55$ km s $^{-1}$ for the GSS inferred from the first of the triple-Gaussian fits above is large compared to previous measurements of ~ 15 km s $^{-1}$ for the dispersion of the GSS (Ibata et al. 2004; Guhathakurta et al. 2006; Kalirai et al. 2006a). In addition, the predicted GSS mean velocities in the F07 model are not as negative as the observed velocities of the GSS. Because of these discrepancies, we carry out an empirical comparison of the f135 velocity distribution to that of the H13s field, which is centered on a high surface brightness portion of the GSS. Field H13s (which is not otherwise analysed in this paper) is located at $\xi = 0.3^\circ$, $\eta = -1.5^\circ$ in Figure 12 and is at approximately the same radial distance along the stream as field f135. In addition to the GSS, the H13s velocity distribution shows a secondary cold component whose origin and physical extent are unknown (Kalirai et al. 2006a). We hereafter refer to the secondary cold component as the “H13s secondary stream.”

The observed mean velocities of the GSS and secondary stream in the H13s field are $\langle v \rangle^{\text{GSS}} = -513$ km s $^{-1}$ and $\langle v \rangle^{\text{sec.str.}} = -417$ km s $^{-1}$, respectively. Each of the cold components has a velocity dispersion of $\sigma_v^{\text{GSS}} = \sigma_v^{\text{sec.str.}} = 16$ km s $^{-1}$ (Kalirai et al. 2006a). The mean

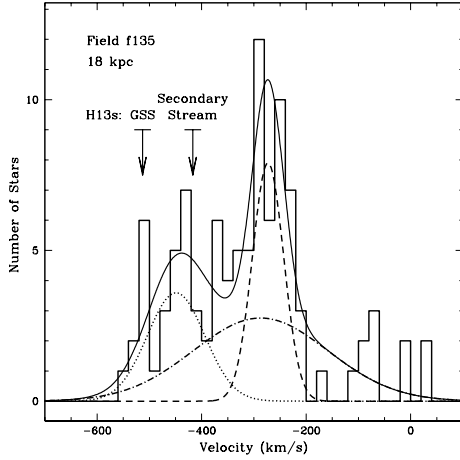


FIG. 14.— Radial velocity histogram of M31 RGB stars in field f135. A triple Gaussian (*solid curve*) has been fit to the observed data using a maximum-likelihood technique, with rough constraints imposed on the parameters based on the properties of the simulated substructure (§ 7.1.3). The wide Gaussian has been held fixed at the best-fit value for the wide component of the combined data: $\langle v \rangle^{\text{sph}} = -287.2 \text{ km s}^{-1}$ and $\sigma_v^{\text{sph}} = 128.9 \text{ km s}^{-1}$ (§ 4.1). The observed velocity distribution is well fit by a sum of three Gaussians: (i) the wide Gaussian which corresponds to the underlying inner spheroid of M31 (*dot-dashed curve*), (ii) a narrow component centered at $\langle v \rangle^{\text{sub}} = -273 \text{ km s}^{-1}$ with a width of $\sigma_v^{\text{sub}} = 30 \text{ km s}^{-1}$, which comprises 30% of the total population and which likely corresponds to the southeast shelf (*dashed curve*), and (iii) a narrow component centered at $\langle v \rangle = -449 \text{ km s}^{-1}$ with a width of $\sigma_v = 55 \text{ km s}^{-1}$, which comprises 25% of the total population and which may correspond to the GSS (*dotted curve*), although it is much wider than previous observations of the GSS ($\sigma_v^{\text{GSS}} \sim 15 \text{ km s}^{-1}$; Ibata et al. 2004; Guhathakurta et al. 2006; Kalirai et al. 2006a). The mean velocity and velocity dispersion ($\pm 1\sigma_v$) of the cold components in field H13s, at a similar radial distance along the GSS as field f135, are shown as arrows and horizontal lines (§ 7.1.3).

velocities and velocity dispersions ($\pm 1\sigma_v$) of these two components are shown as arrows with horizontal lines in Figure 14. It is interesting to note that the first maximum-likelihood triple-Gaussian fit to field f135 does have a secondary $\Delta\chi^2$ minimum with the third peak (GSS component) centered at $\langle v \rangle = -511 \text{ km s}^{-1}$, with $\sigma_v = 8 \text{ km s}^{-1}$ and $N_{\text{GSS}}/N_{\text{tot}} = 0.06$. This hints at the possibility that there may be more than two cold components in this field.

To carry out an empirical comparison of the f135 and H13s velocity distributions, we adopt the above measurements of the mean velocity and velocity dispersion of the GSS and secondary stream in field H13s. These values are held fixed as Gaussian parameters in a constrained fit of the sum of four Gaussians to the data in field f135. A total of five free parameters are fit: (i) the mean velocity, (ii) velocity dispersion, and (iii) fraction of the southeast shelf component, (iv) the fraction of the GSS component, and (v) the fraction of the H13s secondary stream component. The inner spheroid component parameters are held fixed at the usual values. The resulting fractions of substructure are $N_{\text{GSS}}/N_{\text{tot}} = 0.08$, $N_{\text{sec.str.}}/N_{\text{tot}} = 0.07$, and $N_{\text{shelf}}/N_{\text{tot}} = 0.24$. If both the GSS and H13s secondary stream are present in field f135, they appear in equal proportion. For comparison, in H13s the GSS dominates over the secondary stream

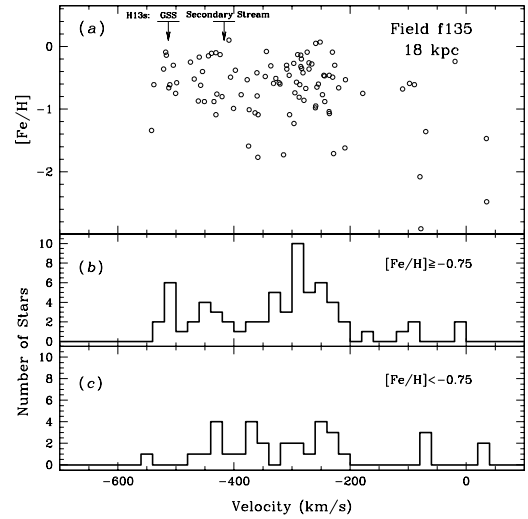


FIG. 15.— (a) Metallicity vs. heliocentric velocity for the M31 RGB stars in field f135, which lies immediately to the east of the edge of the GSS. The mean velocities and dispersions ($\pm 1\sigma_v$) of the GSS and the secondary stream from the nearby field H13s (Kalirai et al. 2006a) are marked, as in Figure 14. (b) Velocity distribution of stars with $[\text{Fe}/\text{H}] > -0.75$. In addition to the cold component at $v_{\text{hel}} \sim -300 \text{ km s}^{-1}$, the metal-rich subset shows evidence of concentrations of stars corresponding to the GSS and secondary stream in the H13s field. (c) Velocity distribution of stars with $[\text{Fe}/\text{H}] < -0.75$. The velocities of stars with metallicities lower than -0.75 dex appear evenly distributed.

by a factor of two (Kalirai et al. 2006a).

Figure 15 shows $[\text{Fe}/\text{H}]$ vs. v_{hel} for the M31 RGB stars in field f135 (panel a), as well as velocity histograms for stars in two $[\text{Fe}/\text{H}]$ bins ($[\text{Fe}/\text{H}] > -0.75$ and $[\text{Fe}/\text{H}] < -0.75$). The mean velocities and velocity dispersions ($\pm 1\sigma_v$) of the cold components (GSS and secondary stream) from field H13s are marked as in Figure 14. The substructure identified with the southeast shelf in this field is metal-rich compared to the spheroid population, and there appears to be 2 metal-rich peaks in the approximate locations of the GSS and secondary stream from H13s. This further hints that there may be as many as three cold components in this field.

In the simulations, the GSS dominates over the southeast shelf in field f135 by about a factor of 10: the observations indicate that, at best, these two populations are roughly equal. The simulations predict that the GSS should comprise a total of 35% of the population in field f135, which is somewhat larger than the fraction of the total population in the most negative cold component from the triple-Gaussian fit shown in Figure 14 (25%). If the “GSS” component from the triple-Gaussian fit is actually comprised of two narrower streams, the GSS comprises a much smaller percentage of the stars in this field than predicted by the simulations.

7.1.4. Predicted Contamination from the GSS in Field a0

The previous section demonstrated that debris from the GSS may be present in field f135, although at a lower level than predicted in the F07 simulations. Debris associated with the GSS is predicted to be present in all of our fields, although it is evident from Figure 12 that the density of GSS debris is expected to fall off precipitously as one moves farther away from the eastern edge

of the GSS. Since the density of M31 RGB spheroid stars drops off strongly with radius in the inner spheroid, and the density of the GSS does not decrease with radius, field a0 represents the most likely minor-axis field in the present study in which to detect GSS debris. Aside from field f135, which is near the edge of the GSS in the simulations, none of our other fields show evidence for significant contamination from the GSS.

The simulated GSS debris in field a0 has a mean and dispersion of $\langle v \rangle_{\text{GSS}} = -364 \text{ km s}^{-1}$ and $\sigma_v^{\text{GSS}} = 32 \text{ km s}^{-1}$. The radial velocity distribution of field a0 shows a population of stars at velocities $< -300 \text{ km s}^{-1}$ in excess of the single-Gaussian fit, and it is *possible* that some of these stars are debris from the GSS. The radial velocity distribution of a0 is consistent with being drawn from a single Gaussian (§ 4.2), although the mean of the distribution is significantly more negative than the mean of the inner spheroid component (-319 km s^{-1} vs. -287 km s^{-1}): the two values of $\langle v \rangle$ are inconsistent at the $\sim 3\sigma$ level.

Figure 16 shows $[\text{Fe}/\text{H}]$ vs. v_{hel} for stars in field a0 (panel *a*), as well as the velocity distributions of stars in two $[\text{Fe}/\text{H}]$ bins ($[\text{Fe}/\text{H}] > -0.75$ and $[\text{Fe}/\text{H}] < -0.75$). The mean velocity and velocity dispersion ($\pm 1\sigma_v$) of the simulated GSS particles are shown as an arrow and horizontal line, respectively. There are a handful of metal-rich stars at the predicted velocity of the GSS. Most of the stars at large negative velocities that appear in excess of the single Gaussian fit are in fact metal-poor. Since debris from the GSS is relatively metal-rich (Fig. 11), this allows us to place a likely upper limit on the contamination of field a0 by the GSS of $\lesssim 5$ stars ($\lesssim 6\%$). In contrast, in the F07 simulations the GSS dominates the M31 spheroid by a factor of ~ 1.6 in the a0 field. We don't have a full understanding of the lopsidedness in Fig 16(*c*); this field has only 75 stars, and the selection of spectral targets was different for this field than the rest of the fields presented in this paper (§ 2.2.1), which makes a direct $[\text{Fe}/\text{H}]$ comparison with other fields difficult.

The GSS is observed to have an asymmetric shape, with a sharp edge on the eastern side and a more gradual decline in density on the western side (McConnachie et al. 2003). Although the F07 simulations reproduce many of the observations in the GSS, they predict a much larger amount of debris on the eastern side than is observed in our fields. Many factors can influence the structure of the debris in the simulations, including the shape and rotation of the progenitor. The current models of the stream (F07) use a spherical, non-rotating progenitor. A more complex model of the progenitor may be required to reproduce the observations.

Previous observational studies have suggested the possibility of substructure along M31's southeast minor axis. Reitzel & Guhathakurta (2002) found a dynamically cold grouping of 4 metal-rich M31 RGB stars (out of ~ 35) along a southeast minor-axis field at $R_{\text{proj}} \sim 19 \text{ kpc}$. This hint of substructure was strengthened by subsequent observations at 7 and 11 kpc along the southeast minor axis, which increased the total M31 RGB sample to ~ 100 stars (Guhathakurta 2002). The star-count maps in Ferguson et al. (2002) (their Fig. 2) also show hints of a population of metal-rich stars along the

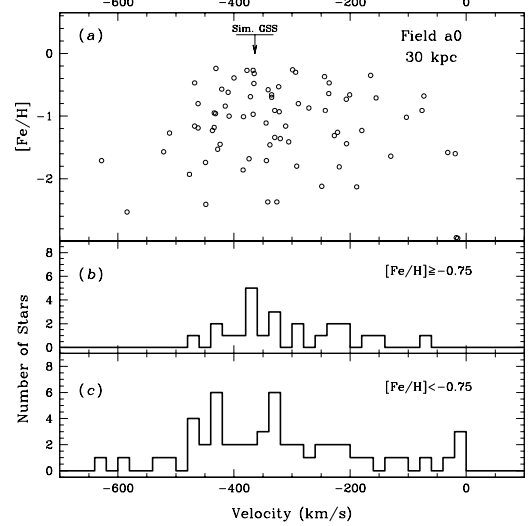


FIG. 16.— Same as Figure 15 for the outermost field a0 at $R_{\text{proj}} \sim 30 \text{ kpc}$. The mean velocity and dispersion ($\pm 1\sigma_v$) of the simulated GSS particles in the F07 simulation are marked by the arrow and horizontal line in (a). There appears to be a handful of metal-rich stars at the velocity predicted for the GSS in the simulations. By contrast, there is no prominent grouping of stars at the velocity of the GSS among metal poor stars. If GSS contamination is present in this field, it is at the level of only a few ($\lesssim 5$) stars.

southeast minor-axis, and deep HST/ACS imaging has discovered a significant intermediate-age population in field H11 (§ 8, Brown et al. 2003). With a spectroscopic sample of 1000 stars, we are able to confidently identify a cold component along the southeast minor axis and characterize its properties, which are in excellent agreement with the predictions of the southeast shelf in the F07 simulations.

7.2. Extended Stellar Disk

The substructure discovered in fields H11, f116 and f123 is centered at close to the systemic velocity of M31 ($v_{\text{sys}} = -300 \text{ km s}^{-1}$), which is the radial velocity expected for an M31 disk component on the minor axis. Recent observational evidence suggests that the disk of M31 is very large, extending to $R \sim 40 \text{ kpc}$ (Reitzel et al. 2004; Ibata et al. 2005). Reitzel et al. (2004) detected M31's stellar disk in a field near the prominent G1 clump, at a radial distance in the plane of the disk of $R \sim 40 \text{ kpc}$. Ibata et al. (2005) present spectroscopy of RGB stars in a number of fields surrounding M31, and show that there is a cold component with velocities close to the expected disk circular velocity in many of their fields, with a typical velocity dispersion of $\sim 30 \text{ km s}^{-1}$. In light of these observations, it is worth discussing whether the substructure we have discovered could be a part of the extended disk of M31.

Ibata et al. (2005) found a smooth disklike structure ranging from $R_{\text{disk}} = 15$ to 40 kpc , at which point they observe a break in the stellar density profile. The substructure in our fields would be at radial distances of 51 to 83 kpc in the plane of the disk; this is beyond the break radius of 40 kpc. Based on the position of the H11 field in the plane of the disk (51 kpc) compared to its relative position in the spheroid of M31, the amount of (smooth) disk contamination is expected to be $< 1\%$ based on a

scale length for the disk of ≈ 5 kpc (Brown et al. 2006a; Walterbos & Kennicutt 1988). The larger scale length proposed by Ibata et al. (2005) of 6.6 kpc would not raise the expected disk contamination to the observed substructure fraction of 44% in field H11. The simulations by F07 include a disk with a scale radius of $R_d = 5.40$ kpc (the heavy concentration of particles close to 0 km s^{-1} in Figure 13, extending outward to -0.73°). The collection of stars between -0.55° and -0.7° correspond to the position of our innermost field, f109. We see no evidence of a similar structure in the observed velocity distribution of this field (Fig. 9).

Although the evidence above suggests it is unlikely that the cold component is part of a smooth disklike structure in our fields, it could still be part of an extended rotating component in the outer disk. Ibata et al. (2005) detect groups of stars moving at the disk circular velocity in fields out to $R_{\text{disk}} = 70$ kpc. It is possible that the substructure observed in our minor axis fields actually represents multiple isolated debris structures in the extended disk of M31. It would require a bit of a cosmic conspiracy to arrange isolated disk debris structures along the minor axis, with a strong trend in velocity dispersion with distance. The structure in field f123 would also be more distant in the plane of the disk than any other structure discovered so far.

The distance of our fields in the plane of the disk and the spatial trends observed in the kinematics of the substructure argue against a disk origin. However, if the disk of M31 has a significant warp, as suggested by observations of the Northern Spur (Walterbos & Kennicutt 1988; Ferguson et al. 2002) and H1 (Roberts 1966; Innanen et al. 1982; Brinks & Burton 1984; Walterbos & Kennicutt 1988; Braun 1991), the effective disk radii of our fields could be decreased (or increased) significantly.

The strongest argument against a disk origin for the discovered substructure is a comparison of the stellar populations in the area of the observed substructure and in fields in the disk of M31. If the cold component is debris associated with M31's extended disk, its stellar population would be expected to have somewhat similar properties to M31's disk. Based on deep HST/ACS imaging, Brown et al. (2006b) show that the derived star formation history of their disk field is distinctly different from the derived star formation history in H11. They find that the disk field is significantly more metal-rich than H11, and has a significantly younger population. In addition, obviously disturbed sections of M31's disk (e.g., the Northern Spur and the G1 clump) show evidence of recent star formation (~ 3 Gyr ago in the Northern Spur and ~ 250 Myr ago in the G1 clump Ferguson et al. 2005). In the Brown et al. (2003, 2006b) H11 field, few of the stars are younger than 4 Gyr. In addition, Brown et al. (2006a) find remarkable agreement between the stellar populations of the H11 field and a field on the GSS (discussed further in § 8).

In conclusion, the observations disfavor an extended rotating disk model for the physical origin of the substructure presented in this paper. The most natural explanation for the origin of the observed minor-axis substructure is tidal debris in the inner spheroid of M31 from a past merging event. Considering the agreement

between the distribution in velocity vs. minor-axis distance of the observed substructure and that predicted to exist in these fields based on the F07 model (§ 7.1), as well as the agreement between the predicted edge of the shell feature and the edge in the CFHT starcount image, it is likely that the substructure is tidal debris from the progenitor of the GSS, in the form of a southeastern shelf.

8. IMPLICATIONS FOR THE INTERMEDIATE-AGE SPHEROID POPULATION

Brown et al. (2003, 2006a,b) present HST/ACS photometry of fields in M31 down to 1-1.5 magnitudes below the main-sequence turnoff. Our field H11 (Fig. 2) is coincident with the Brown et al. (2003) spheroid field. The photometry presented in Brown et al. (2006a) is from a field on the GSS of Andromeda at a projected radial distance of 20 kpc, and is coincident with the Keck/DEIMOS spectroscopy field H13s presented in Kalirai et al. (2006a), and shown in Figure 12 ($\xi = 0.3^\circ$, $\eta = -1.5^\circ$). In the “smooth” spheroid field, Brown et al. (2003) find that $\sim 30\%$ (by mass) of the stellar population is intermediate-age (6–8 Gyr) and metal-rich, while another 30% of the population is old (11–13.5 Gyr) and metal-poor. Brown et al. (2006a) find remarkable agreement in the CMDs of the stream and spheroid fields, indicating that the two fields have very similar age and metallicity distributions. They query whether the similarities between the populations could “be explained by the stream passing through the spheroid field,” but note that this explanation is problematic. It is not likely that H11 happens to be a “chance intersection” with the stream's orbit. In addition, the stream would have to dominate the spheroid by the same factor in both fields (3:1 based on a kinematical analysis of the stream field H13s; Kalirai et al. 2006a), but the kinematical profiles of the two fields are distinctly different, with the H11 field failing to show the cold ($\sigma_v = 16 \text{ km s}^{-1}$) signature of the stream seen in the H13s field. However, they presciently suggested that the similarity in the two populations (spheroid and stream) implies that “the inner spheroid is largely polluted by material stripped from either the stream's progenitor or similar objects.”

In light of the substructure presented in this paper, this seems to be the correct interpretation of the similarity between the “spheroid” and GSS stellar populations. The spatial and kinematic properties of the substructure suggest that the region of the spheroid imaged in the original HST field (Brown et al. 2003) is in fact contaminated by stars from the progenitor of the GSS. The kinematical signature of the substructure at the minor-axis distance of the HST/ACS field (H11) is both predicted (Fig. 13) and observed (Fig. 9) to be relatively wide, and thus less obvious against the background hot component. In the context of the F07 simulations, the minor-axis substructure is not isolated, but is part of one of a series of shells caused by the disruption of the GSS' progenitor, which collectively contaminate a large part of the inner spheroid of M31 (Fig. 12).

The current analysis suggests that $\sim 45\%$ of the M31 RGB stars in the H11 field are in fact part of a cold component, and not part of the broad spheroid. In the H13s field, 75% of the M31 RGB stars are part of a cold

component (Kalirai et al. 2006a). This difference in substructure fraction agrees nicely with the difference in the fraction of intermediate-age (< 10 Gyr), metal-rich stars found in the stream and spheroid fields in Brown et al. (2006b): 70% vs. 40%, respectively. However, recent HST/ACS observations of a field in the location of our f130 masks at 21 kpc imply that this is not the end of the story: Brown et al. (2007) find that the stellar population in H11 can *not* be fit by a linear combination of the GSS (H13s) and the 21 kpc spheroid (f130) stellar populations, due largely to the presence of a greater number of stars younger than 8 Gyr in H11 than in the GSS field. Nevertheless, the observational evidence, combined with the theoretical predictions of F07, strongly favor the explanation that the age and metallicity distributions of the stream and spheroid HST fields are so remarkably similar because the same progenitor polluted both fields with substructure.

9. SUMMARY

The use of the diagnostic method described in Gilbert et al. (2006) has enabled us to isolate the first sample of spectroscopically confirmed M31 RGB stars defined *without* the use of radial velocity. We use this sample of ~ 1000 M31 RGB stars to measure the velocity dispersion of the inner spheroid of M31; in the radial range $R_{\text{proj}} = 9 - 30$ kpc the inner spheroid has a velocity dispersion of $\sigma_v^{\text{sph}} = 129$ km s $^{-1}$. Our data show no evidence of a decrease in the velocity dispersion over this radial range.

The stellar radial velocity distribution in these fields shows evidence of significant amounts of substructure. Compared to the large velocity dispersion seen in the underlying hot spheroid population, the substructure is kinematically cold, exhibiting a decrease in velocity dispersion with increasing projected radius. In the fields in which the feature is observed, $\approx 41\%$ of the stars are estimated to belong to the cold component; the rest are members of the hot inner spheroid of M31. The metallicity of the substructure is higher than that of the broad spheroidal component in the fields in which it is observed.

It is unlikely this cold component is part of the extended disk of M31, given the large radial distance of these fields in the plane of the disk ($\sim 51 - 83$ kpc) and the mismatch in the ages and metallicity of the stellar populations observed in disk fields and field H11. The most plausible physical origin of the substructure discovered in this paper is tidal debris stripped from the progenitor of the GSS. The data agree very well with the location and kinematical properties of the southeast shelf predicted by the F07 simulations of the disruption of the GSS' progenitor. If this is indeed the source of the substructure discovered in this paper, the current observations will add significant observational constraints to those already existing from the GSS, northeast shelf, and western shelf, enabling detailed modeling of M31's dark matter distribution (F07). The minor-axis fields also place constraints on the spatial distribution of the GSS itself. The GSS contamination in our minor-axis fields

is much smaller than predicted by the current models of the stream (F07), which suggests the stream's progenitor had a more complex structure than the simple spherical, non-rotating models so far.

The newly-discovered substructure sheds light on the discovery of a significant intermediate-age population in the "smooth" spheroid field H11 by Brown et al. (2003), and the subsequent discovery of the similarity in ages and metallicities of the stars in the spheroid field, H11, and the giant southern stream field, H13s (Brown et al. 2006a,b). The spheroid HST/ACS field was not in fact placed on a "smooth" spheroid field, and the intermediate-age population may be part of the substructure observed in this field. If the substructure identified in this paper is indeed from the same progenitor as the giant southern stream, it is not surprising that the two HST/ACS fields would have very similar age and metallicity distributions. Given the number of observed fields in the inner spheroid which are contaminated by substructure, both in the current work and in the literature (Irwin et al. 2005; Ferguson et al. 2005; Kalirai et al. 2006a), it seems likely that the inner spheroid is highly contaminated by tidal debris. A "smooth" inner spheroid field may in fact be a rarity.

We are grateful to Sandy Faber and the DEIMOS team for building an outstanding instrument and to Mike Rich for his role in the acquisition of many of the Keck/DEIMOS masks. We thank Peter Stetson, Jim Hesser, and James Clem for help with the acquisition and reduction of CFHT/MegaCam images, Phil Choi, Alison Coil, George Helou, Drew Phillips, and Greg Wirth for observing some DEIMOS masks on our behalf, Drew Phillips for help with slitmask designs, Jeff Lewis, Bill Mason, and Matt Radovan for fabrication of slit-masks, and the DEEP2 team for allowing us use of the `spec1d/zspec` software. We also thank Tom Brown for stimulating discussions and comments on the draft. The `spec2d` data reduction pipeline for DEIMOS was developed at UC Berkeley with support from NSF grant AST-0071048. This project was supported by an NSF Graduate Fellowship (K.M.G.), NSF grants AST-0307966 and AST-0507483 and NASA/STScI grants GO-10265.02 and GO-10134.02 (P.G., K.M.G., and J.S.K.), NSF grant AST-0205969 and NASA ATP grants NAGS-13308 and NNG04GK68G (M.F.), NSF grants AST-0307842 and AST-0307851, NASA/JPL contract 1228235, the David and Lucile Packard Foundation, and The F. H. Levinson Fund of the Peninsula Community Foundation (S.R.M., J.C.O., and R.J.P.), and NSF grant AST-0307931 (D.B.R.). J.S.K. is supported by NASA through Hubble Fellowship grant HF-01185.01-A, awarded by the Space Telescope Science Institute, which is operated by the Association of Universities for Research in Astronomy, Incorporated, under NASA contract NAS5-26555.

APPENDIX

These appendices are intended to give the interested reader more insight into the origin of the differences in the distributions of the M31 RGB samples shown in Figure 3 (§ A.1). The amount of contamination vs. completeness for

different $\langle L_i \rangle$ thresholds is discussed in § A.2. Finally, in § A.3 we quantify the effect of the dwarf contamination on the radial velocity distributions for the M31 RGB sample used in this analysis.

A.1 Effect of the Radial Velocity Diagnostic

As discussed in § 3, empirical probability distribution functions (PDFs) based on training sets of M31 RGB and MW dwarf stars are used to determine the probability that an individual star is an M31 red giant (P_{giant}) or MW dwarf (P_{dwarf}) in 4 (5 for field a0) diagnostics. These probabilities are used to compute the likelihood a star i is a red giant in a given diagnostic j :

$$L_{ij} = \log \left(\frac{P_{\text{giant}}}{P_{\text{dwarf}}} \right). \quad (1)$$

A star's overall likelihood of being an M31 RGB star is defined as

$$\langle L_i \rangle = \frac{\sum_j w_j L_{ij}}{\sum_j w_j}. \quad (2)$$

All available diagnostics for a star are given a weight of one, unless the star is an outlier with respect to both the M31 RGB and MW dwarf PDFs in a two-dimensional diagnostic, in which case the weight of that diagnostic is reduced (§ 3.3 of Gilbert et al. 2006).

Figure 17 shows the overall likelihood distributions for each field, both with ($\langle L_i \rangle$, dashed histogram) and without ($\langle L_i \rangle_{\text{f}}$, solid histogram) the radial velocity diagnostic included in the computation. In general, stars with $\langle L_i \rangle > 0.5$ are designated secure M31 red giants and stars with $\langle L_i \rangle < -0.5$ are designated secure MW dwarfs, while stars with $0 < \langle L_i \rangle < 0.5$ are designated marginal M31 red giants and stars with $-0.5 < \langle L_i \rangle < 0$ are designated marginal MW dwarfs (§ 3.5 of Gilbert et al. 2006).

Figure 3 shows the radial velocity distributions of several combinations of stars: only secure M31 RGB stars, secure and marginal M31 RGB stars, and secure M31 RGB stars plus all stars that are classified as marginal (M31 red giants and MW dwarfs), chosen by use of the diagnostic method both with and without the radial velocity diagnostic. Radial velocity is the most powerful single diagnostic, with a large range of $P_{\text{giant}}/P_{\text{dwarf}}$ values (e.g., Fig. 10 and § 3.4 of Gilbert et al. 2006), and the ability to significantly boost the combined likelihood values. Thus, when the radial velocity diagnostic is not included in the overall likelihood calculation, the $\langle L_i \rangle_{\text{f}}$ values are in general smaller, as can be seen in Figure 17. This causes the significant decrease in the number of secure M31 RGB stars seen in the top panel of Figure 3.

Stars near and more negative than the systemic velocity of M31 have a particularly high probability of being M31 RGB stars in the radial velocity diagnostic: stars with $v_{\text{hel}} = -250 \text{ km s}^{-1}$ have an $L_v = 2$ while stars with $v_{\text{hel}} < -300 \text{ km s}^{-1}$ have $L_v = 5$. Consequently, the velocity diagnostic has a large affect on the $\langle L_i \rangle$ values of these stars, and they are statistically the most affected by removing the radial velocity diagnostic from the overall likelihood calculation. Stars that have velocities in the range over which the radial velocity distributions of the M31 RGB and MW dwarf stars overlap ($\approx -200 < v_{\text{hel}} < -125 \text{ km s}^{-1}$) will have likelihood values near 0 in the radial velocity diagnostic. This means two things: (1) since the L_v value is near zero, it adds no power to the $\langle L_i \rangle$ determination, and thus the number of objects classified as secure M31 RGB stars should be similar regardless of whether or not the radial velocity diagnostic is used, and (2) since these stars do not have the power of the radial velocity diagnostic, they are statistically more likely to land in the marginal ($-0.5 < \langle L_i \rangle < 0.5$) regime. The first effect can be seen in both the top and middle panels of Figure 3, and the second effect can be seen by comparing the numbers of stars in the shaded/dotted histogram in the range $-200 < v_{\text{hel}} < -125 \text{ km s}^{-1}$ in the top, middle, and bottom panels.

The shifting of the overall likelihood distributions to smaller absolute $\langle L_i \rangle$ values due to the removal of the radial velocity diagnostic also increases the numbers of marginal MW dwarf stars (and correspondingly decreases the number of secure MW dwarf stars). As in the case of the secure M31 RGB stars, removing the radial velocity diagnostic from the overall likelihood calculation will have the largest effect on stars that have radial velocities close to or more positive than the peak of the dwarf distribution (observed to be at $v_{\text{hel}} \approx -50 \text{ km s}^{-1}$ in our data set; e.g., Fig. 2 of Gilbert et al. 2006). This causes stars that otherwise would be classified as secure MW dwarf stars to fall into the marginal ($-0.5 < \langle L_i \rangle_{\text{f}} < 0.5$) or even secure ($\langle L_i \rangle_{\text{f}} > 0.5$) M31 RGB regime, depending on the likelihood values of the other diagnostics. This boosts the number of stars in this velocity range in the M31 RGB samples selected without the inclusion of the radial velocity diagnostic.

A.2 Selection of the M31 RGB Sample

Figure 3 shows that there is no difference in the velocity distributions of secure ($\langle L_i \rangle > 0.5$) and secure plus marginal ($\langle L_i \rangle > 0.0$) M31 RGB stars with $v_{\text{hel}} < -300 \text{ km s}^{-1}$, chosen with the use of the radial velocity diagnostic. Since there is minimal MW dwarf contamination at velocities this negative, we assume that the number of M31 RGB stars with $\langle L_i \rangle > 0$ (465 stars) represents the true number of M31 RGB stars observed in this velocity range. This allows a calculation of the level of incompleteness in other samples. There are 446 stars with $v_{\text{hel}} < -300 \text{ km s}^{-1}$ and $\langle L_i \rangle_{\text{f}} > 0$; this sample is 96% complete. Samples selected using the thresholds $\langle L_i \rangle_{\text{f}} > [0.5, 0.75, \text{ and } 1]$ are [78%, 57%, and 26%] complete.

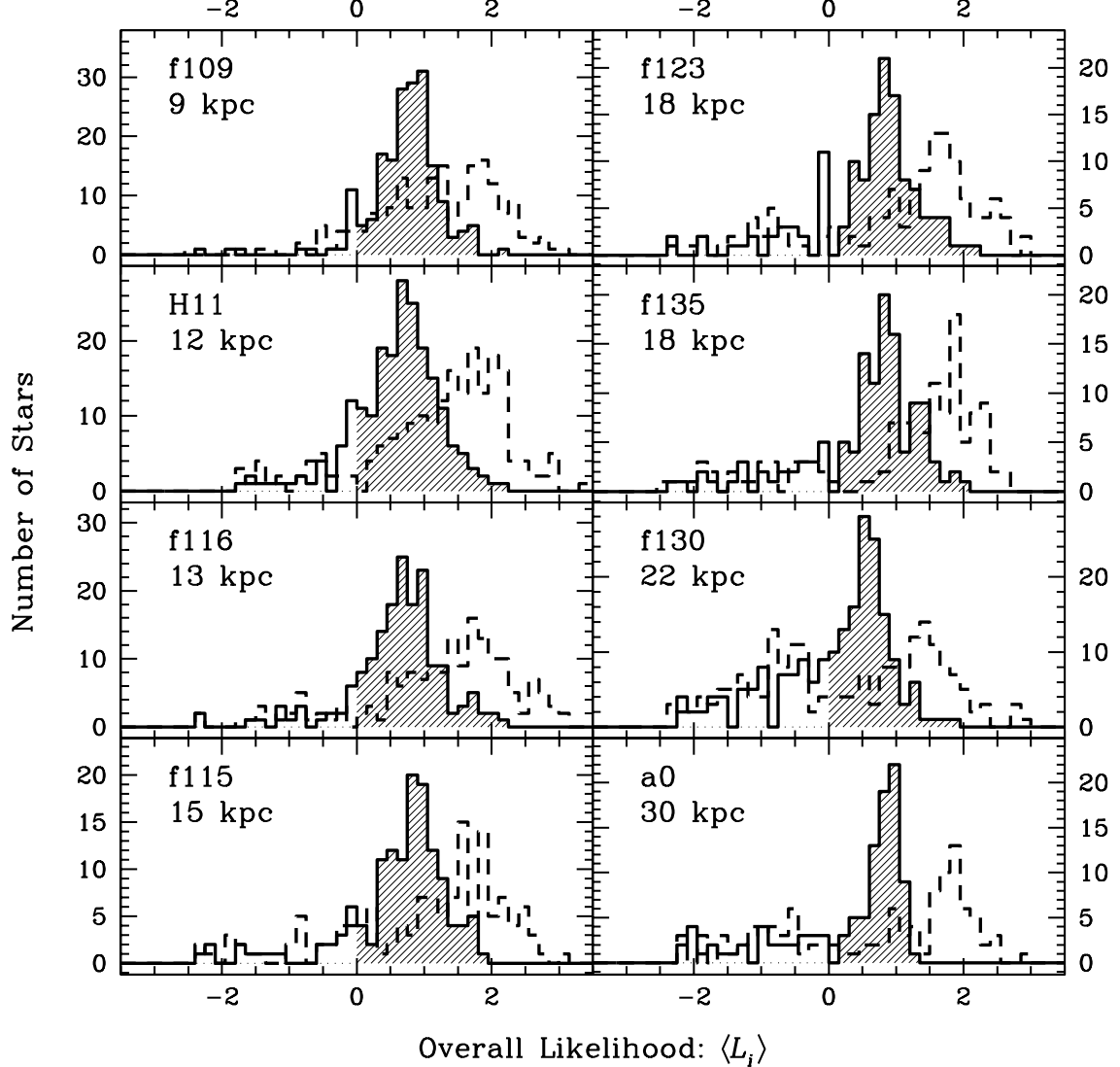


FIG. 17.— Overall likelihood distributions with ($\langle L_i \rangle$, dashed) and without ($\langle L_i \rangle_{\phi}$, solid) the inclusion of the radial velocity diagnostic. The analysis in this paper is based on the sample of M31 RGB stars shown by the shaded histograms. For stars with $\langle L_i \rangle > 0$, removal of the radial velocity diagnostic from the $\langle L_i \rangle$ calculation causes a shift in the peak of the distribution from $\langle L_i \rangle \approx 2$ to $\langle L_i \rangle \approx 1$. This is to be expected, since radial velocity is the most powerful of the five diagnostics. A similar shift of the peak of the distribution towards $\langle L_i \rangle = 0$ likely occurs for stars with $\langle L_i \rangle < 0$, however the numbers of stars in this category is too small for this shift to be easily discernible.

The vast majority of the dwarf contaminants will have $v_{\text{hel}} > -150 \text{ km s}^{-1}$. Counts of stars in this velocity range for a given sample, compared to an estimate of the expected number of M31 RGB stars in this velocity range, gives an estimate of the level of dwarf contamination. The thresholds $\langle L_i \rangle_{\phi} > 0.75$ and $\langle L_i \rangle_{\phi} > 1$ are quite severe, requiring that a star have a probability of being an M31 RGB star that is 5 or 10 times higher than its probability of being an MW dwarf star, respectively. These samples are assumed to have minimal dwarf contamination. Based on the numbers of stars with $v_{\text{hel}} > -150 \text{ km s}^{-1}$ that pass these $\langle L_i \rangle_{\phi}$ thresholds (41 stars for $\langle L_i \rangle_{\phi} > 0.75$ and 22 stars for $\langle L_i \rangle_{\phi} > 1$) and the completeness factors calculated above, a complete sample of M31 RGB stars would have approximately 76 stars at $v_{\text{hel}} > -150 \text{ km s}^{-1}$. A sample selected using the threshold $\langle L_i \rangle_{\phi} > 0.5$ has 66 stars, which is 87% complete. However, the $\langle L_i \rangle_{\phi} > 0.5$ sample is expected to be only 78% complete, implying that 9% of the stars with $v_{\text{hel}} > -150 \text{ km s}^{-1}$ in this sample are MW dwarf star contaminants (overall, this sample has a 1.9% contamination rate). A similar calculation for stars selected using the $\langle L_i \rangle_{\phi} > 0$ threshold yields a contamination rate of $\sim 40\%$ for stars with $v_{\text{hel}} > -150 \text{ km s}^{-1}$. This large local contamination rate corresponds to a 5.0% contamination rate for the entire sample. A parallel calculation using the number of stars with $v_{\text{hel}} > -200 \text{ km s}^{-1}$ yields similar overall contamination rates, confirming that the majority of the MW dwarf contamination is at $v_{\text{hel}} > -150 \text{ km s}^{-1}$. The majority of the dwarf contamination comes from blue stars [panel (d) of Fig. 10], since the Na I, CMD, and [Fe/H] diagnostics are all less sensitive for blue stars (§ 4.1.2 of Gilbert et al. 2006).

The focus of this paper is the substructure discovered along the southeast minor axis of M31. Therefore, we have chosen to use the most complete M31 RGB sample chosen without the use of radial velocity, $\langle L_i \rangle_\phi > 0$, as it gives the most robust statistics for the cold component, even though it suffers from significant MW dwarf contamination at velocities near zero. The removal of the radial velocity diagnostic yields a sample composed of an underlying, kinematically unbiased M31 RGB population, as well as a contaminating MW dwarf population at velocities near zero. For the analysis presented in this paper, this is preferable to a clean, but kinematically biased M31 RGB sample, as the effect of the MW dwarf contamination on the measured properties of the M31 RGB sample can be quantified by analysing samples chosen using stricter $\langle L_i \rangle_\phi$ thresholds.

A.3 Bias in Measured Spheroid Velocity

The main effect of the MW dwarf contamination in our chosen M31 RGB sample ($\langle L_i \rangle_\phi > 0$) is a positive shift in the measured mean velocity of the spheroidal distribution. This shift will affect the measured $\langle v \rangle^{\text{sph}}$ in the double-Gaussian fit to the combined sample (§ 4.1), and the $\langle v \rangle^{\text{sph}}$ values from the single-Gaussian fits to individual fields (§ 4.2). The substructure component is cold enough that its measured properties are not significantly affected by the dwarf contamination. As discussed above (§ A.2), the amount of MW dwarf contamination is small in the $\langle L_i \rangle_\phi > 0.5$ sample and minimal in the $\langle L_i \rangle_\phi > 0.75$ sample. Although these samples suffer from significant incompleteness (22% and 43%, respectively), they are large enough to allow a measurement of the underlying spheroidal component. Maximum-likelihood double-Gaussian fits to the $\langle L_i \rangle_\phi > 0.5$ and $\langle L_i \rangle_\phi > 0.75$ samples yield $\langle v \rangle^{\text{sph}}$ values of $-302.5^{+7.7}_{-8.3}$ and $-309.6^{+10.8}_{-8.7}$ km s $^{-1}$, respectively. The best-fit σ_v^{sph} values for the two samples are $123.3^{+8.3}_{-7.0}$ and $128.3^{+10.8}_{-8.7}$ km s $^{-1}$, respectively. Thus, the best-fit $\langle v \rangle^{\text{sph}}$ values from the $\langle L_i \rangle_\phi > 0$ sample should be adjusted by ~ 15 to 20 km s $^{-1}$ to account for the MW dwarf contamination in the sample. This makes the $\langle v \rangle^{\text{sph}}$ value from the best-fit double Gaussian ($\langle v \rangle^{\text{sph}} = -287.2$ km s $^{-1}$) consistent with the systemic velocity of M31 ($v_{\text{sys}} = -300$ km s $^{-1}$). Although dwarf contamination is expected to increase with radius due to the decreasing surface density of M31 stars, there is little difference in the mean offset of $\langle v \rangle^{\text{sph}}$ if the sample is split by radius into inner and outer bins.

REFERENCES

Abraham, R. G., van den Bergh, S., Glazebrook, K., Ellis, R. S., Santiago, B. X., Surma, P., & Griffiths, R. E. 1996, ApJS, 107, 1A

Barnes, J. E., & Hernquist, L. 1992, ARA&A, 30, 705

Battaglia, G., Helmi, A., Morrison, H., Harding, P., Olszewski, E. W., Freeman, K. C., Norris, J., Shectman, S. A. 2005, MNRAS, 364, 433

Bertin, E., & Arnouts, S. 1996, A&AS, 117, 393

Braun, R. 1991, ApJ, 372, 54

Brinks, E. & Burton, W. B. 1984, A&A, 141, 195

Brown, T. M., Ferguson, H. C., Smith, E., Kimble, R. A., Sweigart, A. V., Renzini, A., Rich, R. M., & Vandenberg, D. A. 2003, ApJ, 592, L17

Brown, T. M., Smith, E., Guhathakurta, P., Rich, R. M., Ferguson, H. C., Renzini, A., Sweigart, A. V., & Kimble, R. A. 2006, ApJ, 636, L89

Brown, T. M., Smith, E., Ferguson, H. C., Rich, R. M., Guhathakurta, P., Renzini, A., Sweigart, A. V., & Kimble, R. A. 2006, ApJ, 652, 323

Brown, T. M., Smith, E., Ferguson, H. C., Guhathakurta, P., Kalirai, J. S., Rich, R. M., Renzini, A., Sweigart, A. V., Reitzel, D., Gilbert, K. M., & Geha, M. 2007, ApJ, in press (astro-ph/0702448)

Bullock, J. S., & Johnston, K. V. 2005, ApJ, 635, 931

Bullock, J. S., Kravtsov, A. V., & Weinberg, D. H. 2001, ApJ, 548, 33

Chapman, S. C., Ibata, R., Lewis, G. F., Ferguson, A. M. N., Irwin, M., McConnachie, A., & Tanvir, N. 2006, ApJ, 653, 255

Choi, P. I., Guhathakurta, P., & Johnston, K. V. 2002, AJ, 124, 310

Conselice, C. J., Bershady, M. A., Dickinson, M., & Papovich, C. 2003, AJ, 126, 1183

Croton, D. J., Springel, V., White, S. D. M., De Lucia, G., Frenk, C. S., Gao, L., Jenkins, A., Kauffmann, G., Navarro, J. F., & Yoshida, N. 2006, MNRAS, 365, 11

de Vaucouleurs, G. 1958, ApJ, 128, 465

Dekel, A., Stoehr, F., Mamon, G. A., Cox, T. J., Novak, G. S., & Primack, J. R. 2005, Nature, 437, 707

Durrell, P. R., Harris, W. E., & Pritchett, C. J. 2004, AJ, 128, 260

Fardal, M. A., Babul, A., Geehan, J. J., & Guhathakurta, P. 2006, MNRAS, 366, 1012F

Fardal, M. A., Guhathakurta, P., Babul, A., & McConnachie, A. W. 2007, MNRAS, submitted (astro-ph/0609050) [F07]

Fellhauer, M., Belokurov, V., Evans, N. W., Wilkinson, M. I., Zucker, D. B., Gilmore, G., Irwin, M. J., Bramich, D. M., Vidrih, S., Wyse, R. F. G., Beers, T. C., & Brinkmann, J. 2006, ApJ, 651, 167

Ferguson, A. M. N., Irwin, M. J., Ibata, R. A., Lewis, G. F., & Tanvir, N. R. 2002, AJ, 124, 1452

Ferguson, A. M. N., Johnson, R. A., Faria, D. C., Irwin, M. J., Ibata, R. A., Johnston, K. V., Lewis, G. F., Tanvir, N. R. 2005, ApJ, 622, L109

Ferguson, A. M. N., Chapman, S., Ibata, R. A., Irwin, M. J., Lewis, G. F., McConnachie A. W. 2006, in Stanghellini, L., Walsh J. R., Douglas N. G., eds, Planetary Nebulae beyond the Milky Way. Springer-Verlag, Berlin, 286

Font, A. S., Johnston, K. V., Guhathakurta, P., Majewski, S. R., & Rich, R. M. 2006, AJ, 131, 1436

Geehan, J. J., Fardal, M. A., Babul, A., & Guhathakurta, P. 2006, MNRAS, 366, 996G

Gilbert, K. M., Guhathakurta, P., Kalirai, J. S., Rich, R. M., Majewski, S. R., Ostheimer, J. C., Reitzel, D. B., Cenarro, A. J., Cooper, M. C., Luine, C., Patterson, R. J. 2006, ApJ, 652, 1188

Guhathakurta, P. 2002, in "The Shapes of Galaxies and Their Dark Matter Halos", ed. P. Natarajan (Singapore: World Scientific), 162

Guhathakurta, P., Ostheimer, J. C., Gilbert, K. M., Rich, R. M., Majewski, S. R., Kalirai, J. S., Reitzel, D. B., & Patterson, R. J. 2005, arXiv preprint (astro-ph/0502366)

Guhathakurta, P., Rich, R. M., Reitzel, D. B., Cooper, M. C., Gilbert, K. M., Majewski, S. R., Ostheimer, J. C., Geha, M. C., Johnston, K. V., & Patterson, R. J. 2006b, AJ, 131, 2497

Helmi, A., & White, S. D. M. 1999, MNRAS, 307, 495

Helmi, A., & de Zeeuw, T. 2000, MNRAS, 319, 657

Helmi, A. 2004, ApJ, 610, L97

Hernquist, L., & Quinn, P. J. 1998, ApJ, 331, 682

Holland, S. 1998, AJ, 115, 1916

Ibata, R., Chapman, S., Ferguson, A. M. N., Irwin, M., Lewis, G., & McConnachie, A. 2004, MNRAS, 351, 117

Ibata, R., Chapman, S., Ferguson, A. M. N., Lewis, G., Irwin, M., & Tanvir, N. 2005, ApJ, 634, 287

Ibata, R. A., Gilmore, G., & Irwin, M. J. 1994, Nature, 370, 194

Ibata, R., Lewis, G. F., Irwin, M. J., Totten, E., & Quinn, T. 2001a, ApJ, 551, 294

Ibata, R., Irwin, M. J., Ferguson, A. M. N., Lewis, G., & Tanvir, N. 2001b, Nature, 412, 49

Innanen, K. A., Kamper, K. W., Papp, K. A., & van den Bergh S. 1982, ApJ, 254, 515

Irwin, M. J., Ferguson, A. M. N., Ibata, R. A., Lewis, G. F., & Tanvir, N. R. 2005, ApJ, 628, 105

Johnston, K. V., Hernquist, L., & Bolte, M. 1996, ApJ, 465, 278

Johnston, K. V. 1998, ApJ, 495, 297

Johnston, K. V., Hongsheng, Z., Spergel, D. N., & Hernquist, L., 1999, ApJ, 512, 109

Johnston, K. V., Spergel, D. N., & Haydn, C. 2002, *ApJ*, 570, 656

Johnston, K. V., Law, D. R., & Majewski, S. R. 2005, *ApJ*, 619, 800

Kalirai, J. S., Guhathakurta, P., Gilbert, K. M., Reitzel, D. B., Rich, R. M., Majewski, S. R., & Cooper, M. C. 2006a, *ApJ*, 641, 268

Kalirai, J. S., Gilbert, K. M., Guhathakurta, P., Majewski, S. R., Ostheimer, J. C., Rich, R. M., Cooper, M. C., Reitzel, D. B., & Patterson, R. J. 2006b, *ApJ*, 648, 389

Law, D. R., Johnston, K. V., & Majewski, S. R. 2005, *ApJ*, 619, 807L

LeFevre, O., Abraham, R., Lilly, S. J., Ellis, R. S., Brinchmann, J., Schade, D., Tresse, L., Colless, M., Crampton, D., Glazebrook, K., Hammer, F., & Broadhurst, T. 2000, *MNRAS*, 311, 565L

Lotz, J. M., Davis, M., Faber, S. M., Guhathakurta, P., Gwyn, S., Huang, J., Koo, D. C., Le Floc'h, E., Lin, L., Newman, J., Noeske, K., Papovich, C., Willmer, C. N. A., Coil, A., Conselice, C. J., Cooper, M., Hopkins, A. M., Metevier, A., Primack, J., Rieke, G., & Weiner, B. J. 2007, *ApJ*, submitted (astro-ph/0602088)

Majewski, S. R., Ostheimer, J. C., Kunkel, W. E., & Patterson, R. J. 2000, *AJ*, 120, 2550

Majewski, S. R., Skrutskie, M. F., Weinberg, M. D., & Ostheimer, J. C. 2003, *ApJ*, 599, 1082

Mamon, G. A., & Lokas, E. L. 2005, *MNRAS*, 363, 705

Martínez-Delgado, D., Gómez-Flechoso, M. Á., Aparicio, A., & Carrera, R. 2004, *ApJ*, 601, 242

Mathewson, D. S., Cleary, M. N., & Murray, J. D. 1974, *ApJ*, 190, 291

McConnachie, A. W., Irwin, M. J., Ibata, R. A., Ferguson, A. M. N., Lewis, G. F., & Tanvir, N. R. 2003, *MNRAS*, 343, 1335

Merrett, H. R., Kuijken, K., Merrifield, M. R., Romanowsky, A. J., Douglas, N. G., Napolitano, N. R., Arnaboldi, M., Capaccioli, M., Freeman, K. C., Gerhard, O., Evans, N. W., Wilkinson, M. I., Halliday, C., Bridges, T. J. & Carter, D. 2003, *MNRAS*, 346, L62

Merrett, H. R., Merrifield, M. R., Douglas, N. G., Kuijken, K., Romanowsky, A. J., Napolitano, N. R., Arnaboldi, M., Capaccioli, M., Freeman, K. C., Gerhard, O., Coccato, L., Carter, D., Evans, N. W., Wilkinson, M. I., Halliday, C., & Bridges, T. J. 2006, *MNRAS*, 369, 120

Merrifield, M. R., & Kuijken, K. 1998, *MNRAS*, 297, 1292

Mould, J. & Kristian, J. 1986, *ApJ*, 316, 517

Navarro, J. F., Frenk, C. S., & White, S. D. M. 1996, *ApJ*, 462, 563

Navarro, J. F., et al. 2004, *MNRAS*, 349, 1039

Newberg, H. J., et al. 2003, *ApJ*, 596, L191

Ostheimer, J. C. 2002, Ph.D. thesis, University of Virginia

Peñarrubia, J., Benson, A. J., Martínez-Delgado, D., & Rix, H. W. 2006, *ApJ*, 645, 240

Pritchett, C. J., & van den Bergh, S. 1994, *AJ*, 107, 1730

Palma, C., Majewski, S. R., Siegel, M. H., Patterson, R. J., Ostheimer, J. C., & Link, R. 2003, *AJ*, 125, 1352

Reitzel, D. B., & Guhathakurta, P. 2002, *AJ*, 124, 234

Reitzel, D. B., Guhathakurta, P., & Rich, R. M. 2004, *AJ*, 127, 2133

Rocha-Pinto, H. J., Majewski, S. R., Skrutskie, M. F., & Crane, J. D. 2003, *ApJ*, 594, L115

Roberts, M. S. 1966, *ApJ*, 144, 639

Schweizer, F. 1980, *ApJ*, 279, 596

Searle, L., & Zinn, R. 1978, *ApJ*, 225, 357

Sohn, S. T., Majewski, S. R., Muñoz, R. R., Kunkel, W. E., Johnston, K. V., Ostheimer, J. C., Guhathakurta, P., Patterson, R. J., Siegel, M. H., Cooper, M. C. 2007, *ApJ*, submitted (astro-ph/0608151)

Springel, V., White, S. D. M., Jenkins, A., Frenk, C. S., Yoshida, N., Gao, L., Navarro, J., Thacker, R., Croton, D., Helly, J., Peacock, J. A., Cole, S., Thomas, P., Couchman, H., Evrard, A., Colberg, J., & Pearce, F. 2005, *Nature*, 435, 629

Stanek, K. Z., & Garnavich, P. M. 1998, *ApJ*, 503, L131

VandenBerg, D. A., Bergbusch, P. A., & Dowler, P. D. 2006, *ApJS*, 162, 375

Walterbos, R. A. M., & Kennicutt, R. C., Jr. 1988, *A&A*, 198, 61

White, S. D. M., & Rees, M. J. 1978, *MNRAS*, 183, 341

Yanny, B., et al. 2003, *ApJ*, 588, 824

